

Riemann solver with internal reconstruction (RSIR) for compressible single-phase and non-equilibrium two-phase flows

Quentin Carmouze^(1,2), Richard Saurel^(2,3), Alexandre Chiapolino⁽³⁾ and Emmanuel Lapebie⁽⁴⁾

⁽¹⁾ University of Nice, LJAD UMR CNRS 7351, Parc Valrose, 06108 Nice Cedex, France

⁽²⁾ Aix Marseille Univ, CNRS, Centrale Marseille, LMA, Marseille, France

⁽³⁾ RS2N SAS, Saint Zacharie, France

⁽⁴⁾ APEX Solutions SAS, Flaujac, France

Abstract

A new Riemann solver is built to address numerical resolution of complex flow models. The research direction is closely linked to a variant of the Baer and Nunziato (1986) model developed in Saurel et al. (2017a). This recent model provides a link between the Marble (1963) model for two-phase dilute suspensions and dense mixtures. As the Marble model, the Saurel et al. one is weakly hyperbolic with the same 4 characteristic waves, while the system involves 7 partial differential equations. It implies serious theoretical and practical issues rendering the building of a simple and accurate flow solver difficult. To overcome related difficulties the Riemann solver of Linde (2002) is revisited. The method is first examined in the simplified context of the compressible Euler equations. Physical considerations are introduced in the solver improving robustness and accuracy of the Linde method. With these modifications, accuracy is shown to be comparable to the one of the HLLC solver of Toro et al. (1994). Second the two-phase flow model is considered. A locally conservative formulation is built and validated, removing issues related to the non-conservative terms. However, two extra major issues arise from numerical experiments. The solution appears not self-similar and multiple contact waves emerge in the dispersed phase. The design of a Riemann solver is consequently challenging. The modified Linde method is thus examined for the considered flow model. Some basic properties of the equations are used, such as shock relations of the dispersed phase and jump conditions across the contact wave. Thanks to these ingredients the new Riemann solver with internal reconstruction (RSIR), modification of the Linde method, handles stationary volume fraction discontinuities, presents low dissipation for transport waves and handles shocks and expansion waves accurately. It is validated on various test problems showing method's accuracy and versatility for complex flow models. Its capabilities are illustrated on a difficult two-phase flow instability problem, unresolved before.

Keywords: two-phase, dense-dilute, weakly hyperbolic, Riemann solver

I. Introduction

The present contribution addresses the building of a robust Riemann solver with limited dissipation for complex flow models. The reconstruction method of Linde (2002) is revisited and improved in terms of accuracy and robustness. This effort is mainly motivated by the numerical approximation of a two-phase non-equilibrium flow model developed by the authors that involves a series of theoretical challenges, presented in the following. In the present introduction the modelling context is recalled first, and the numerical approach is introduced secondly.

Modelling context

It is well accepted that hyperbolic models are mandatory to deal with phenomena involving wave propagation. This is the case for multiphase flows in many situations such as in particular shock and detonation propagation in granular explosives and in fuel suspensions, as well as liquid-gas mixtures with bubbles, cavitating and flashing flows, as soon as motion is intense and governed by pressure gradients. This is thus the case in most unsteady two-phase flow situations.

Wave propagation is important as it carries pressure, density and velocity disturbances. Sound propagation is also very important as it determines critical (choked) flow conditions and associated mass flow rates. It has also fundamental importance for sonic conditions of detonation waves when the two-phase mixture is exothermically reacting (Petitpas et al., 2009).

Hyperbolicity is also related to the causality principle, meaning that initial and boundary conditions are responsible for time evolution of the solution. When dealing with first-order partial differential equations it means that the Riemann problem (RP) must have a solution, and the RP is correctly posed only if the equations are hyperbolic.

However, only a few two-phase flow models are hyperbolic in the whole range of parameters. The Baer and Nunziato (1986) model (BN) seemed to be the only formulation able to deal with such requirement. However, in the dilute limit at least, the acoustic properties of this model seemed inconsistent (Lhuillier et al., 2013). Indeed, with this model, the dispersed phase sound speed corresponds to the one of the pure phase, while this phase is not continuous and unable to propagate sound in reality, at least at a scale larger than a particle. When the phase is not continuous (dispersed drops in a gas, dispersed bubbles in a liquid), the associated sound speed should vanish, such effect being absent in the formulation.

When the particle volume concentration reaches the lower limit (typically of the order of 1% or less) the Marble (1963) model is preferred. This model corresponds to the Euler equations with source terms for the gas phase and pressureless gas dynamic equations for the particle phase (see also Zeldovich, 1970). This model is thermodynamically consistent and hyperbolic as well, except that the equations of the particle phase are weakly hyperbolic. In this model, contrarily to the BN model, sound does not propagate in the particle phase, this behaviour being more physical in this limit. However, the Marble model has a limited range of validity as the volume of the dispersed phase is neglected, this assumption having sense only for low volume fractions (less than 1%) of the condensed phase.

Recently, the gap between these two models has been filled (Saurel et al., 2017a). Modifications of the volume fraction equation of the BN model resulted in a flow model where sound propagates only in the carrier phase. The model is hyperbolic with same 4 wave speeds as Marble's one and is thermodynamically consistent in the stiff pressure relaxation limit. Moreover, in the stiff velocity relaxation limit, the Kapila et al. (2001) model, important for diffuse interface computations (Saurel and Pantano, 2018), is recovered.

Saurel et al. (2017a) model has been solved in the same reference with a Godunov-type scheme based on a Rusanov-type (1961) solver. However, as well known, this solver is quite diffusive for stationary discontinuities and linearly degenerate fields, such as volume fraction discontinuities and contact

waves. This is precisely the motivation of the present work, focused on the building of a Riemann solver with enhanced accuracy.

Riemann solver with internal reconstruction (RSIR)

In the quest of Riemann solvers with low dissipation for the present flow model, several issues appear:

- The flow model, as most two-phase flow models, presents non-conservative terms;
- Numerical experiments of typical initial value problems (IVPs) achieved with the Godunov-Rusanov method exhibit non self-similar solutions. Such behavior appears as a combination of non-conservative terms, acting as a drag force (in differential form), and stiff pressure relaxation, mandatory for this specific flow model.
- Governing equations of the dispersed phase are hyperbolic degenerate, as a single eigenvalue is responsible for the propagation of characteristic waves. Therefore, it is impossible to determine a basis of eigenvectors and associated Riemann invariants. Moreover, the solution can be multivalued, as for Marble's model (Saurel et al., 1994). It means that multiple volume fraction waves may be present in the solution, rendering the analysis and design of any Riemann solver intricate.

Several attempts were made by the authors to build an approximate Riemann solver for this flow model on the basis of,

- characteristic relations for the carrier phase and jump conditions for the dispersed one,
- HLLC-type approximation based on a local conservative formulation, that will be presented later.

None of these attempts yielded an efficient solver, at least according to the authors' experiments. They consequently moved to another type of solver, based on internal reconstruction of intermediate states, computed from a simple and robust intercell state, such as Rusanov (1961) or HLL (Harten et al., 1983). This research direction has been investigated by Linde (2002), Miyoshi and Kusano (2005) and many others, mainly in the frame of magnetohydrodynamics (MHD) equations that also involve many waves in the RP. The aim is to build two intermediate states instead of one. Doing so, the method should maintain stationary discontinuities and reduce numerical diffusion during simple transport.

The underlying philosophy of this approach relies on the assumption that most of the physics is present in the two extreme waves and only one contact wave, that has to be identified. If the contact wave cannot be defined clearly, the method becomes irrelevant. But it seems that in most flow models such as the Euler equations, MHD (e.g. Balsara, 2012), compressible solid mechanics (e.g. Gavrilyuk et al., 2008), and the present two-phase model, identification of the contact wave is possible. The remaining waves, when present, are captured by the scheme during computations even if they are omitted in the RP. This is the same philosophy as the Rusanov and HLL solvers, except that an extra intermediate wave is added.

In the present work, the Linde method is revisited. This method is based first on a consistency relation, linking the two intermediate states and the HLL average state and second on an extra heuristic relation, linking the jumps of the two intermediate states across the contact wave. This second relation is reconsidered and approximated on the basis of some physical properties of the equations, in particular regarding thermodynamic transformations.

The paper is organized as follows. The Linde (2002) method is recalled in Section II in its basic version and computational examples are shown with the Euler equations. It sometimes works perfectly, but oscillations appear depending on the initial conditions. This observation motivates reconsideration of the heuristic relation, now based on thermodynamics, resulting in significant improvements and yielding robust and accurate solutions. Accuracy and robustness are shown to be comparable to the HLLC solver.

In Section III the internal reconstruction method is extended to the two-phase flow model of interest. As before extra physics is inserted in the closure relations. The (trivial) Rankine-Hugoniot relations of the dispersed phase are used as well as jump conditions of the carrier phase across the contact wave of the dispersed phase. Thanks to these ingredients the flow solver becomes very efficient. One-dimensional computational examples are shown in the same section.

The method is then embedded in the DALPHADT© unstructured mesh code. It is used to compute fingering instability occurring during explosive dispersion of particle clouds. Such instability seems misunderstood and not reproduced by existing flow models. Intensive experimental and numerical studies were done in this area recently, as for example in Rodriguez et al. (2013), McGrath et al. (2018), Osnes et al. (2018) and Xue et al. (2018). Thanks to the new model and present numerical method, the formation stage of this instability seems correctly predicted, at least qualitatively. Computational examples are shown in Section IV. Conclusions are given in Section V.

II- Riemann solver with internal reconstruction (RSIR) for the Euler equations

The Riemann solver with internal reconstruction is a modification of the Linde (2002) solver. The original Linde solver is recalled in the frame of the Euler equations and modifications are addressed next.

The Euler equations of compressible fluids consist in a system of conservation laws,

$$\frac{\partial \mathbf{U}}{\partial t} + \frac{\partial \mathbf{F}}{\partial x} = 0, \quad (\text{II.1})$$

with $\mathbf{U} = (\rho, \rho \mathbf{u}, \rho \mathbf{E})^T$ and $\mathbf{F} = (\rho \mathbf{u}, \rho \mathbf{u}^2 + \mathbf{p}, (\rho \mathbf{E} + \mathbf{p}) \mathbf{u})^T$ where ρ denotes the density, \mathbf{u} the velocity and $\mathbf{E} = \mathbf{e} + \frac{1}{2} \mathbf{u}^2$ the total energy. The pressure \mathbf{p} is given by a convex equation of state (EOS), as a function for example of internal energy \mathbf{e} and density ρ : $\mathbf{p} = \mathbf{p}(\rho, \mathbf{e})$. The stiffened gas (SG) EOS will be used frequently in the present contribution as,

$$\mathbf{p}(\rho, \mathbf{e}) = (\gamma - 1)\rho \mathbf{e} - \gamma p_\infty,$$

where γ and p_∞ are constants specific to a given fluid. This EOS is retained for the sake of conciseness only. The numerical methods addressed in the present work are valid for any convex EOS.

This system is strictly hyperbolic with wave speeds $\lambda_1 = \mathbf{u}$, $\lambda_2 = \mathbf{u} - \mathbf{c}$ and $\lambda_3 = \mathbf{u} + \mathbf{c}$. The sound speed is defined by $\mathbf{c} = \sqrt{\frac{\partial \mathbf{p}}{\partial \rho}}_s$ where s denotes the entropy.

The various reconstruction methods considered in the present paper are based on the HLL (Harten et al., 1983) approximate solution, or its simplified version due to Rusanov (1961). In the HLL solver, the extreme waves only are used, and their speeds are estimated as (Davis, 1988),

$$\mathbf{S}_L = \min(\mathbf{u}_L - \mathbf{c}_L, \mathbf{u}_R - \mathbf{c}_R) \text{ and } \mathbf{S}_R = \max(\mathbf{u}_L + \mathbf{c}_L, \mathbf{u}_R + \mathbf{c}_R), \quad (\text{II.2})$$

where subscripts L and R denote the left and right states of the initial data of the RP.

The intermediate HLL state is a consequence of the Rankine-Hugoniot relations of System (II.1) applied across the left- and right-facing waves propagating at speeds \mathbf{S}_L and \mathbf{S}_R respectively:

$$\mathbf{U}_{\text{HLL}}^* = \frac{\mathbf{F}_R - \mathbf{F}_L + \mathbf{S}_L \mathbf{U}_L - \mathbf{S}_R \mathbf{U}_R}{\mathbf{S}_L - \mathbf{S}_R}. \quad (\text{II.3})$$

From this state, the aim is now to reconstruct two intermediate states, as illustrated in Figure II.1 and linked through the consistency relation (II.4):

$$(\mathbf{S}_R - \mathbf{S}_L) \mathbf{U}_{\text{HLL}}^* = (\mathbf{S}_R - \mathbf{S}_M) \mathbf{U}_R^* + (\mathbf{S}_M - \mathbf{S}_L) \mathbf{U}_L^*. \quad (\text{II.4})$$

This consistency relation can be rewritten as,

$$U_{HLL}^* = \omega_R U_R^* + \omega_L U_L^*,$$

$$\text{with } \omega_R = \frac{S_R - S_M}{S_R - S_L} \text{ and } \omega_L = \frac{S_M - S_L}{S_R - S_L}.$$

The contact wave speed is given by,

$$S_M = \frac{p_R - p_L + (\rho u)_L (S_L - u_L) - (\rho u)_R (S_R - u_R)}{\rho_L (S_L - u_L) - \rho_R (S_R - u_R)}.$$

Relation (II.4) involves two unknown states, U_L^* and U_R^* . Consequently, an extra relation is needed. Linde (2002) postulate is considered first.

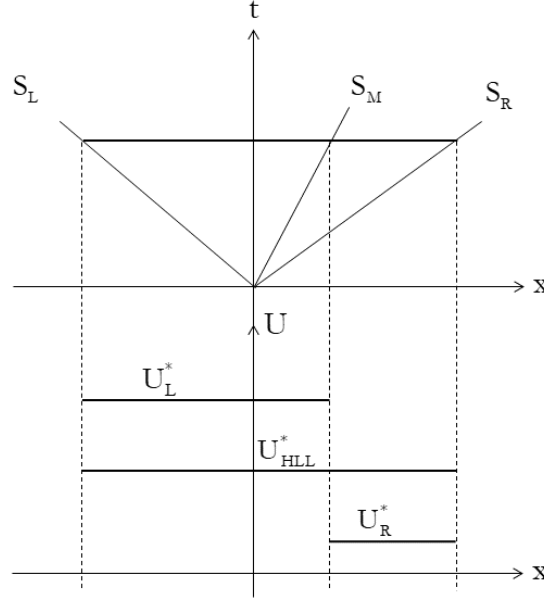


Figure II.1 – Schematic representation of the two intermediate states U_L^* and U_R^* rebuilt from U_{HLL}^* .

II.1 Linde reconstruction

Linde reconstruction is based on the following relation,

$$U_R^* - U_L^* = \beta (U_R - U_L), \quad (II.5)$$

where β represents a viscosity parameter, $0 \leq \beta \leq 1$.

When β is taken equal to zero, the HLL approximation is recovered. When $\beta = 1$ the reconstruction tends to the HLLC representation but is not equivalent, as interface conditions are ignored in the Linde approach. It is worth mentioning that when $\beta = 1$, isolated density discontinuities are preserved, an important property in CFD solvers.

Relation (II.5) is then combined with Relation (II.4) resulting in:

$$\begin{cases} U_L^* = U_{HLL}^* - \omega_R \beta (U_R - U_L), \\ U_R^* = U_{HLL}^* + \omega_L \beta (U_R - U_L). \end{cases} \quad (II.6)$$

Once states U_L^* and U_R^* are computed the various fluxes are determined through the Rankine-Hugoniot relations,

$$\begin{cases} \mathbf{F}_R^* = \mathbf{F}_R + \mathbf{S}_R (\mathbf{U}_R^* - \mathbf{U}_R), \\ \mathbf{F}_L^* = \mathbf{F}_L + \mathbf{S}_L (\mathbf{U}_L^* - \mathbf{U}_L). \end{cases} \quad (\text{II.7})$$

Solution sampling is achieved through,

$$\mathbf{F}^* = \begin{cases} \mathbf{F}_L & \text{if } S_L \geq 0, \\ \mathbf{F}_L^* & \text{if } S_L < 0 \text{ and } S_M \geq 0, \\ \mathbf{F}_R^* & \text{if } S_R > 0 \text{ and } S_M < 0, \\ \mathbf{F}_R & \text{if } S_R \leq 0. \end{cases}$$

Typical solutions obtained with this solver embedded in a Godunov-type code are shown hereafter. Let us first consider the transport of a density discontinuity in a uniform velocity and pressure flow with a gas governed by the ideal gas EOS with $\gamma = 1.4$. Corresponding results are shown in Figure II.2.

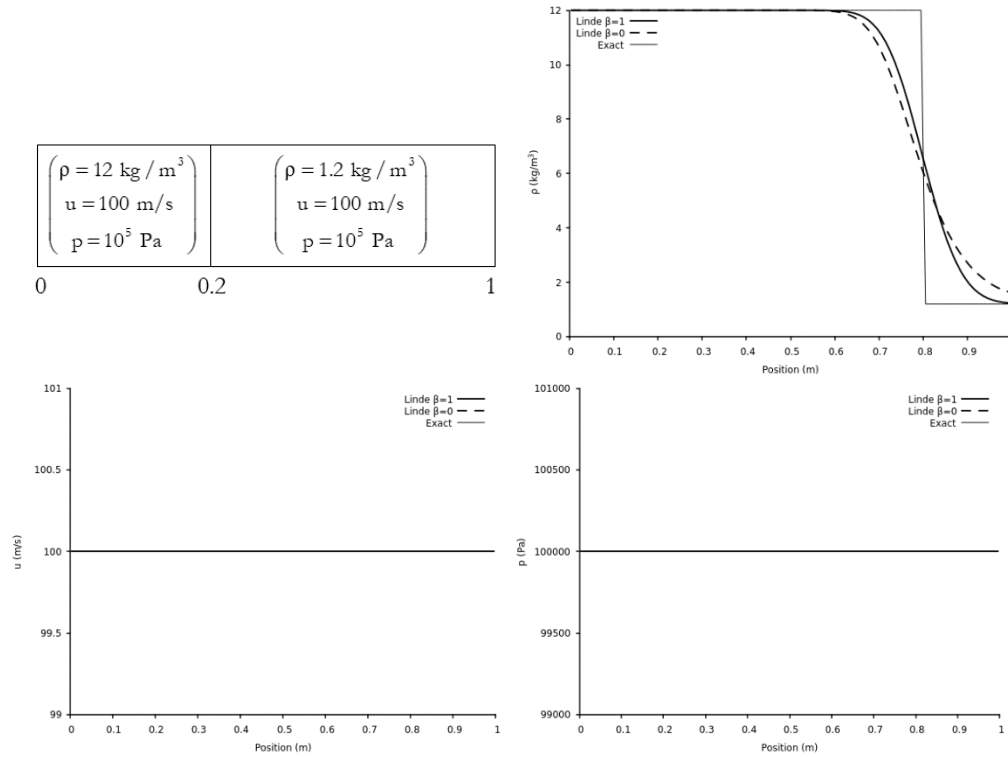


Figure II.2 – Computed results with the original Linde solver for the transport of a density discontinuity in a uniform pressure and velocity flow. The Godunov first-order scheme is used with 100 computational cells and CFL = 0.9. Results are shown at time $t=6$ ms. The density discontinuity is correctly transported, and mechanical equilibrium is maintained. Numerical diffusion is reduced when $\beta = 1$.

Second, a shock tube test problem is examined in Figure II.3.

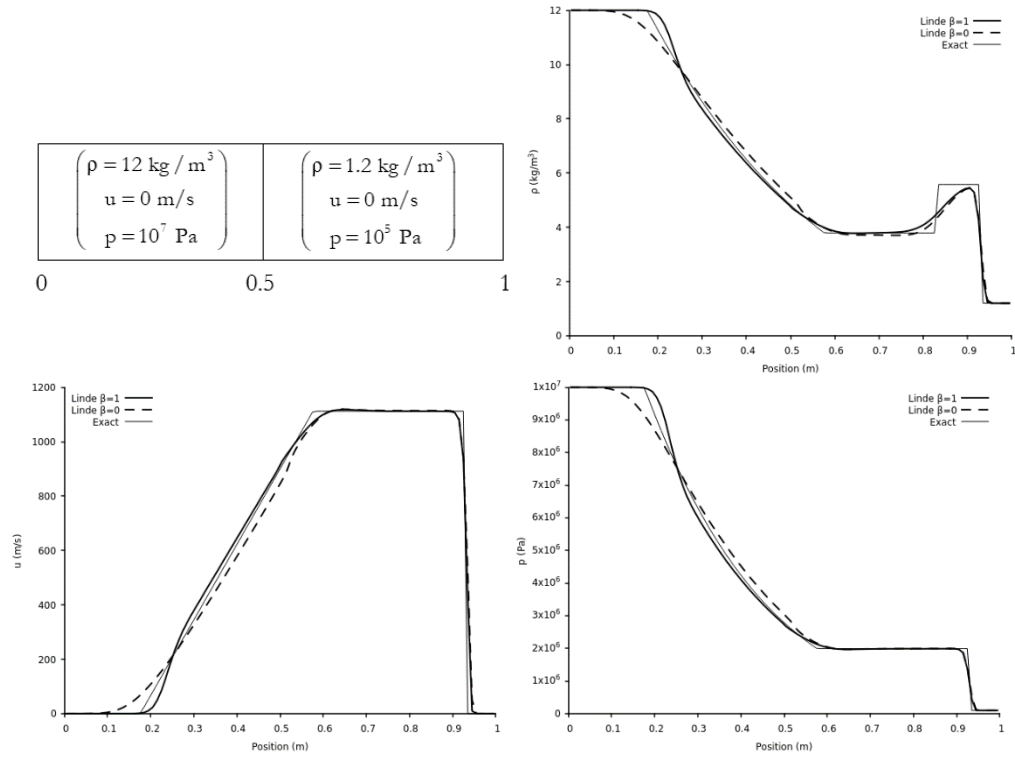
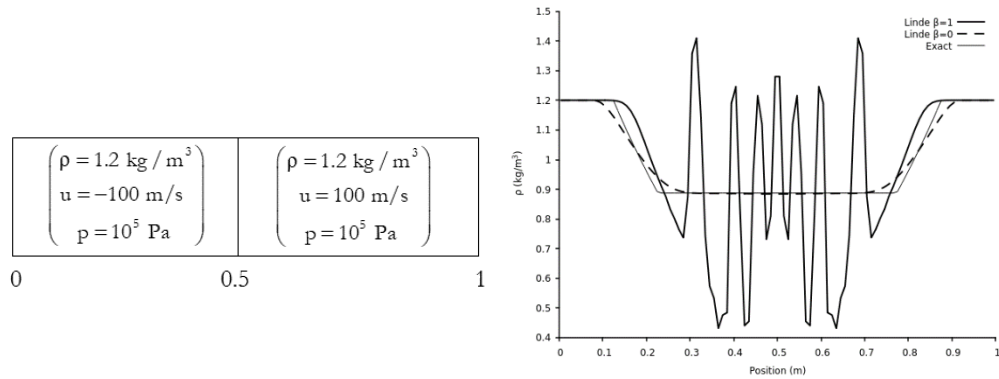


Figure II.3 – Computed results with the original Linde solver for a shock tube test case. The Godunov first-order scheme is used with 100 computational cells and CFL=0.9. Results are shown at time $t=300 \mu\text{s}$. The various waves and states are computed quite correctly.

Third, a double expansion test is considered in Figure II.4.



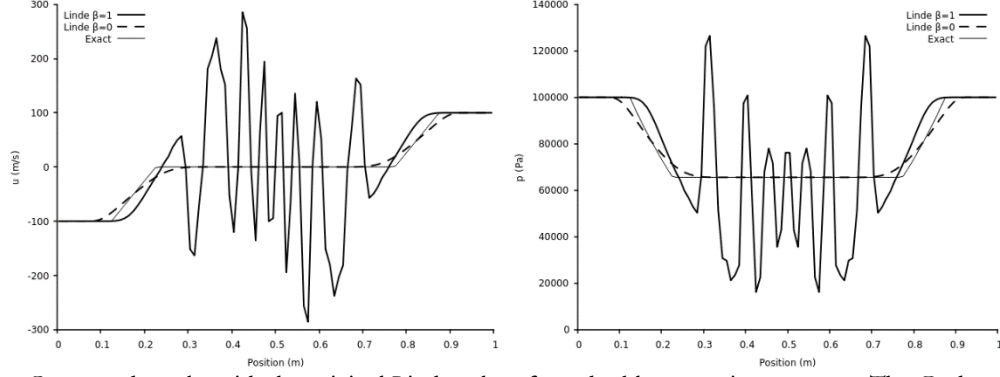


Figure II.4 – Computed results with the original Linde solver for a double expansion test case. The Godunov first-order scheme is used with 100 computational cells and CFL=0.9. Results are shown at time $t=850 \mu\text{s}$. Oscillations appear when $\beta = 1$.

Results of Figure II.4 clearly show limitations of the method when (II.5) is used as a closure relation. Decreasing parameter β (for instance $\beta = 0.5$) makes the method tend to the HLL solver and oscillations are reduced but remain present (at least for this test). When $\beta = 0$ the HLL solution state is recovered and oscillations disappear but deficiencies related to stationary contact discontinuities and transport at constant speed come back.

Same limitations and even more unstable solutions appear for double shock tests, just reversing the velocities in the initial data of the previous test (Figure II.4).

Accuracy of the conventional Linde method is consequently highly dependent on initial data and viscosity parameter β . It is worth mentioning that in Linde (2002) a method is given to determine β as a parameter vector to improve the solution. But it is important to note that as soon as β is strictly less than 1, the solver loses its ability to preserve isolated stationary discontinuities. Modification of this solver is thus addressed in the next paragraph.

II.2 New reconstruction method (RSIR)

The reconstruction derived hereafter is based on two ingredients:

- Quasi-isentropic variations across right- and left-facing waves;
- Interface conditions across the contact wave.

Although considered as rough approximation, in particular across strong shocks, the thermodynamic evolutions through the right- and left-facing waves are approximated as isentropic. The isentropic evolutions are themselves approximated through sound speed definition and trapezoidal approximation as,

$$\bar{c}^2 = \frac{p_R^* - p_R}{\rho_R^* - \rho_R}, \quad (\text{II.8})$$

$$\bar{c}^2 = \frac{p_L^* - p_L}{\rho_L^* - \rho_L},$$

where,

$$\bar{c} = \frac{1}{2}(c_L + c_R).$$

Across the contact wave S_M , the interface pressure condition reads,

$$p_L^* = p_R^* = p^*.$$

System (II.8) becomes,

$$\mathbf{p}^* = \mathbf{p}_R + \bar{c}^2 (\rho_R^* - \rho_R), \quad (\text{II.9})$$

$$\mathbf{p}^* = \mathbf{p}_L + \bar{c}^2 (\rho_L^* - \rho_L).$$

Taking the difference of these two relations, the following one is obtained:

$$\rho_R^* - \rho_L^* = \rho_R - \rho_L - \frac{\mathbf{p}_R - \mathbf{p}_L}{\bar{c}^2}. \quad (\text{II.10})$$

This relation corresponds to a modification of the first relation of System (II.5).

For the sake of generality only, parameter β is introduced as,

$$\rho_R^* - \rho_L^* = \beta \left(\rho_R - \rho_L + \frac{\mathbf{p}_L - \mathbf{p}_R}{\bar{c}^2} \right) = \Psi_{\text{mass}}. \quad (\text{II.11})$$

Indeed, when $\beta = 0$ the HLL approximation $\rho_L^* = \rho_R^*$ is recovered. However, the present RSIR solver is designed to address two distinct intermediate states \mathbf{U}_L^* and \mathbf{U}_R^* in the same mind as the HLLC solver. Consequently either $\beta = 0$ or $\beta = 1$ is considered. The RSIR solver is then parameter free in the sense that either the HLL solution or the RSIR one when $\beta = 1$ is used. In all computational tests addressed in the present contribution, unless stated otherwise, $\beta = 1$.

Combining (II.6) and (II.11) intermediate density states are obtained as,

$$\begin{cases} \rho_L^* = \rho_{\text{HLL}}^* - \omega_R \beta \left(\rho_R - \rho_L + \frac{\mathbf{p}_L - \mathbf{p}_R}{\bar{c}^2} \right), \\ \rho_R^* = \rho_{\text{HLL}}^* + \omega_L \beta \left(\rho_R - \rho_L + \frac{\mathbf{p}_L - \mathbf{p}_R}{\bar{c}^2} \right). \end{cases} \quad (\text{II.12})$$

Determination of the intermediate momentum states is now addressed. From (II.11) similar relation is deduced for momentum jump across the contact wave. As $\mathbf{u}_L^* = \mathbf{u}_R^* = \mathbf{S}_M$, (II.11) implies,

$$(\rho \mathbf{u})_R^* - (\rho \mathbf{u})_L^* = \beta \left(\rho_R - \rho_L + \frac{\mathbf{p}_L - \mathbf{p}_R}{\bar{c}^2} \right) \mathbf{S}_M = \Psi_{\text{momentum}}. \quad (\text{II.13})$$

Combining (II.6) and (II.13) the intermediate momentum states are obtained as,

$$\begin{cases} (\rho \mathbf{u})_L^* = (\rho \mathbf{u})_{\text{HLL}}^* - \omega_R \beta \left(\rho_R - \rho_L + \frac{\mathbf{p}_L - \mathbf{p}_R}{\bar{c}^2} \right) \mathbf{S}_M, \\ (\rho \mathbf{u})_R^* = (\rho \mathbf{u})_{\text{HLL}}^* + \omega_L \beta \left(\rho_R - \rho_L + \frac{\mathbf{p}_L - \mathbf{p}_R}{\bar{c}^2} \right) \mathbf{S}_M. \end{cases} \quad (\text{II.14})$$

Determination of the intermediate energy states is now addressed. As star densities are known from (II.12), star pressures are determined by the same approximate isentropic relations (II.9). Summing the two star pressures (II.9) to preserve symmetry, the following relation is obtained,

$$\mathbf{p}^* = \frac{\mathbf{p}_L + \mathbf{p}_R}{2} + \bar{c}^2 \left(\frac{\rho_L^* + \rho_R^*}{2} - \frac{\rho_L + \rho_R}{2} \right). \quad (\text{II.15})$$

The energy jump across the contact wave is approximated thanks to (II.12) and (II.15) and the EOS,

$$\begin{cases} (\rho E)_L^* = \rho_L^* \left(e(\mathbf{p}^*, \rho_L^*) + \frac{1}{2} \mathbf{S}_M^2 \right), \\ (\rho E)_R^* = \rho_R^* \left(e(\mathbf{p}^*, \rho_R^*) + \frac{1}{2} \mathbf{S}_M^2 \right). \end{cases} \quad (\text{II.16})$$

The energy jump finally reads,

$$(\rho E)_R^* - (\rho E)_L^* = \rho_R^* \left(e(\mathbf{p}^*, \rho_R^*) + \frac{1}{2} S_M^2 \right) - \rho_L^* \left(e(\mathbf{p}^*, \rho_L^*) + \frac{1}{2} S_M^2 \right) = \Psi_{\text{energy}}, \quad (\text{II.17})$$

and the intermediate energy states read,

$$\begin{cases} (\rho E)_L^* = (\rho E)_{\text{HLL}}^* - \omega_R \left[\rho_R^* \left(e(\mathbf{p}^*, \rho_R^*) + \frac{1}{2} S_M^2 \right) - \rho_L^* \left(e(\mathbf{p}^*, \rho_L^*) + \frac{1}{2} S_M^2 \right) \right], \\ (\rho E)_R^* = (\rho E)_{\text{HLL}}^* + \omega_L \left[\rho_R^* \left(e(\mathbf{p}^*, \rho_R^*) + \frac{1}{2} S_M^2 \right) - \rho_L^* \left(e(\mathbf{p}^*, \rho_L^*) + \frac{1}{2} S_M^2 \right) \right]. \end{cases} \quad (\text{II.18})$$

Note that parameter β is included in $\rho_{L,R}^*$. Note also that (II.16) does not depend on the EOS form. Once states \mathbf{U}_L^* and \mathbf{U}_R^* are computed the various fluxes are computed through the Rankine-Hugoniot relations, according to the sign of S_M ,

$$\begin{cases} \mathbf{F}_R^* = \mathbf{F}_R + S_R (\mathbf{U}_R^* - \mathbf{U}_R), \\ \mathbf{F}_L^* = \mathbf{F}_L + S_L (\mathbf{U}_L^* - \mathbf{U}_L). \end{cases}$$

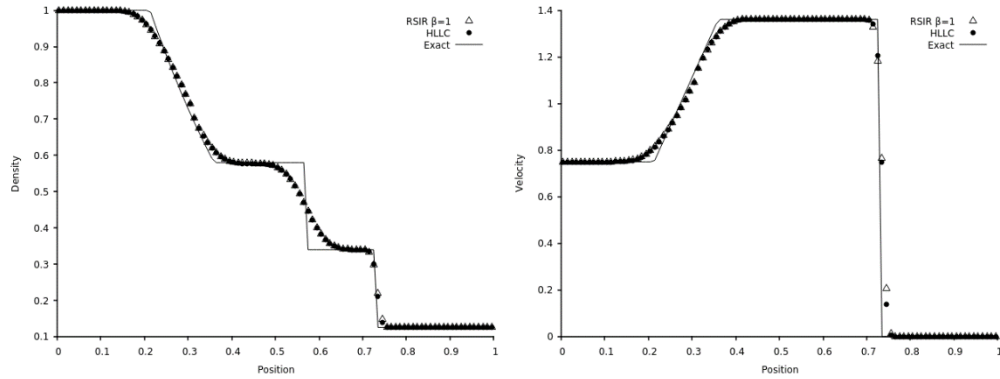
Intermediate states are given by (II.12), (II.14) and (II.18). In compact form they read,

$$\begin{cases} \mathbf{U}_L^* = \mathbf{U}_{\text{HLL}}^* - \omega_R \Psi, \\ \mathbf{U}_R^* = \mathbf{U}_{\text{HLL}}^* + \omega_L \Psi, \end{cases} \quad (\text{II.19})$$

where $\Psi = (\Psi_{\text{mass}}, \Psi_{\text{momentum}}, \Psi_{\text{energy}})^T$, with components given in (II.11), (II.13) and (II.17).

The Riemann solver thus consists in (II.3) for the HLL state determination and (II.19) to rebuild the two intermediate states.

Comparison with the HLLC solver and exact solution is now addressed on various test problems. Let us recall that, unless mentioned otherwise, $\beta = 1$ in all computations. The various test problems are given in Toro (2009, 2019). In addition, the blast wave test problem of Colella and Woodward (1984) is also addressed. Extreme wave speeds are approximated following (II.2) (Davis, 1988) for both solvers (RSIR and HLLC). Computed results are provided in Figures II.5-II.12. In these computations all variables are dimensionless as done in Toro (2009, 2019). Note that these test problems are quite severe except tests 6 and 7 that involve a stationary discontinuity and transport of a discontinuity. Those two last tests are nonetheless essential to assess methods' accuracy.



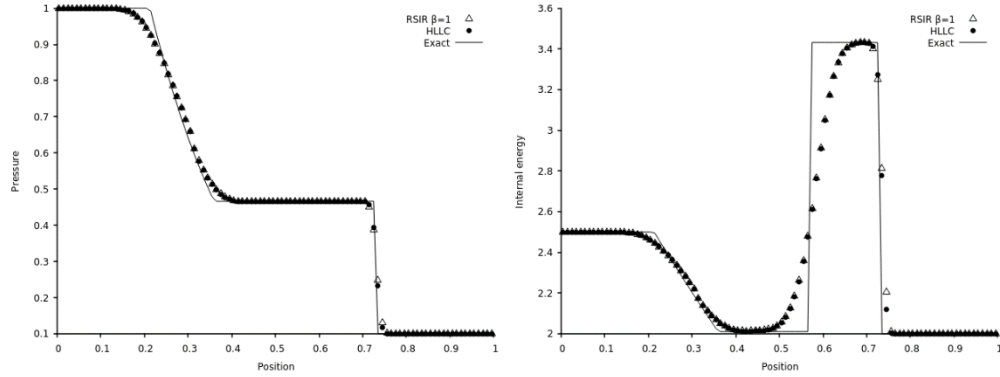


Figure II.5 – Test 1 of Toro (2009) page 334 (shock tube test). Comparison of the RSIR, HLLC and exact solutions. The computational domain involves 100 cells and the Godunov first-order scheme is used with CFL=0.9. Results are shown at time $t=0.2$. The initial discontinuity is located at $x_0 = 0.3$. Both methods show comparable accuracy.

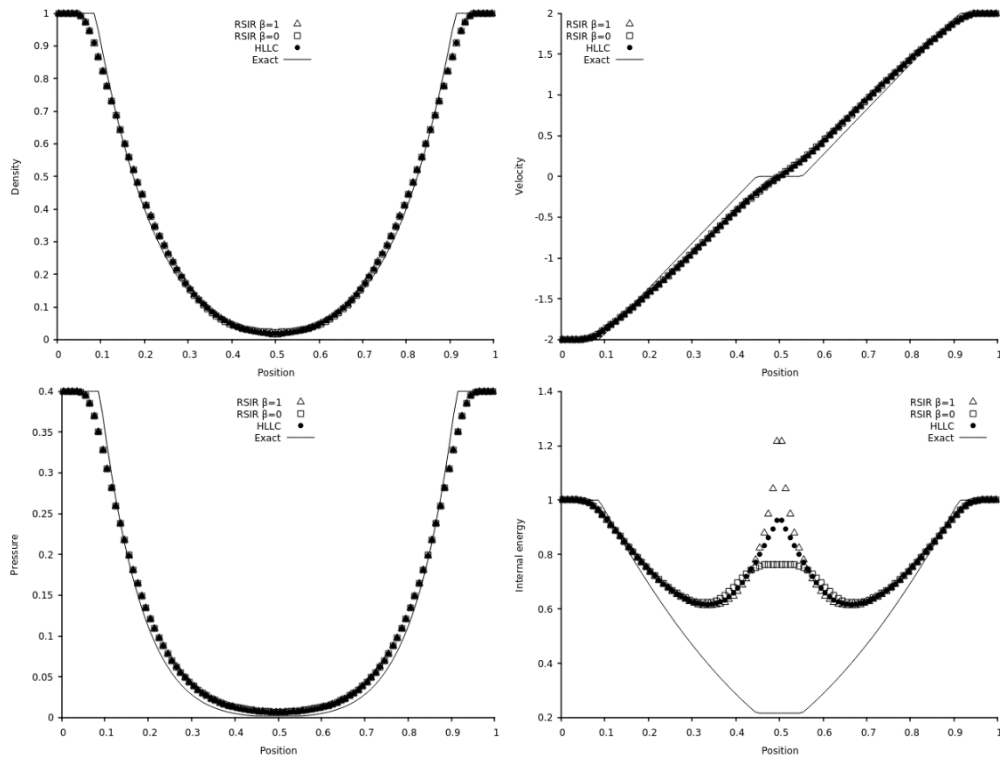


Figure II.6 – Test 2 of Toro (2009) page 334 (double expansion test). Comparison of the RSIR, HLLC and exact solutions. The computational domain involves 100 cells and the Godunov first-order scheme is used with CFL=0.9. Results are shown at time $t=0.15$. The initial discontinuity is at position $x_0 = 0.5$. Both methods produce unphysical overheating at the center of the domain. HLLC results are less inaccurate than RSIR when $\beta = 1$ while RSIR yields less inaccurate results than those of HLLC when $\beta = 0$. The other flow variables are computed correctly. Issues related to overheating do not seem related to the Riemann solver accuracy but more to the computation of the kinetic energy (Cocchi et al., 1998).

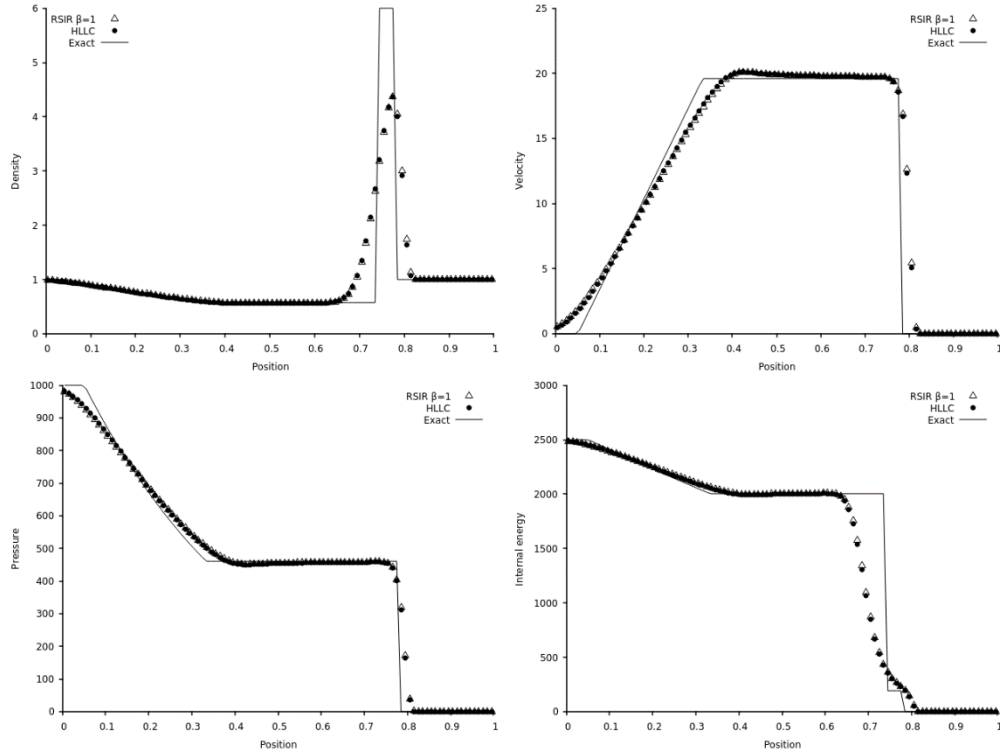


Figure II.7 – Test 3 of Toro (2009) page 334 (strong shock tube test). Comparison of the RSIR, HLLC and exact solutions. The computational domain involves 100 cells and the Godunov first-order scheme is used with CFL=0.9. Results are shown at time $t=0.012$. The initial discontinuity is located at $x_0 = 0.5$. Both methods show comparable accuracy.

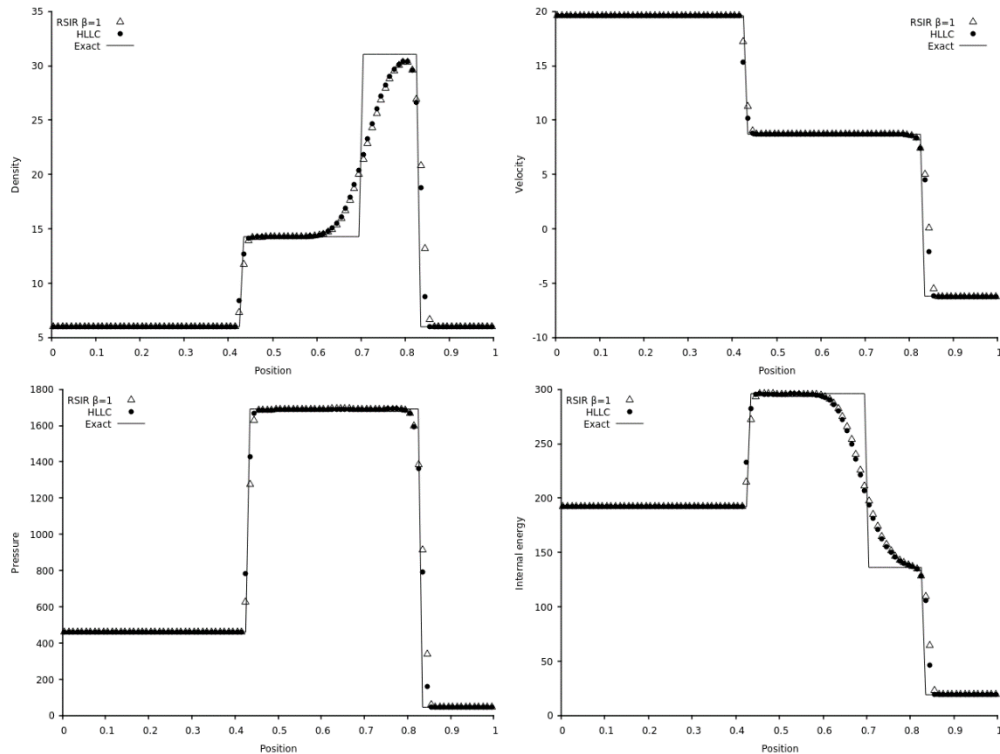


Figure II.8 – Test 4 of Toro (2009) page 334 (double shock test). Comparison of the RSIR, HLLC and exact solutions. The computational domain involves 100 cells and the Godunov first-order scheme is used with CFL=0.9. Results are shown at time $t=0.035$. The initial discontinuity is located at $x_0 = 0.4$. Both methods show comparable accuracy.

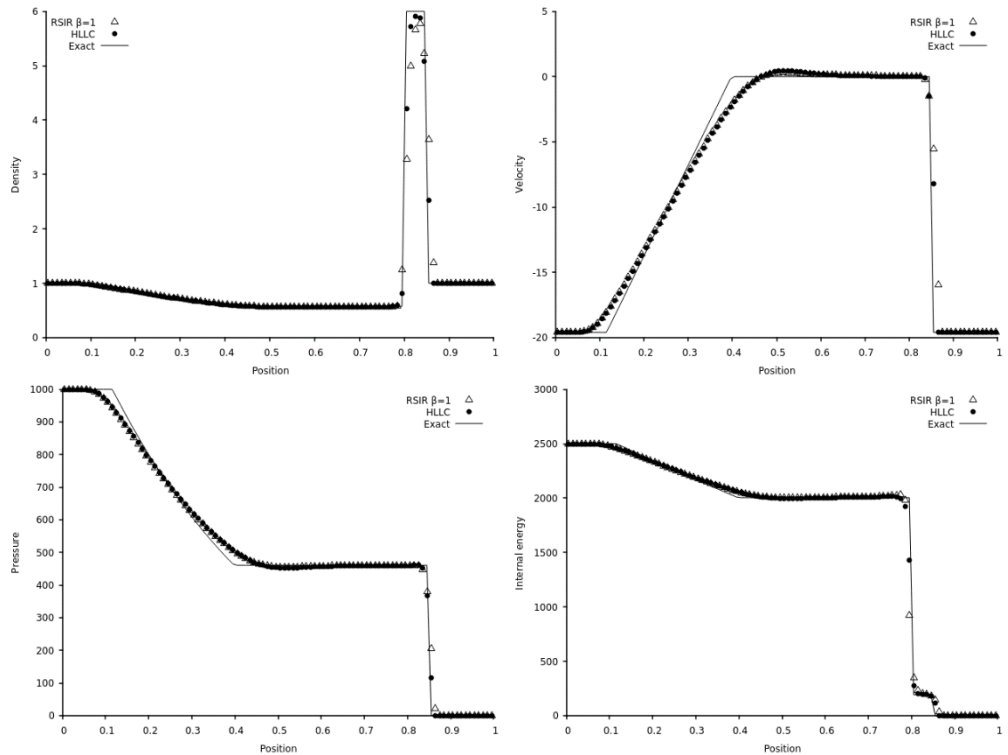
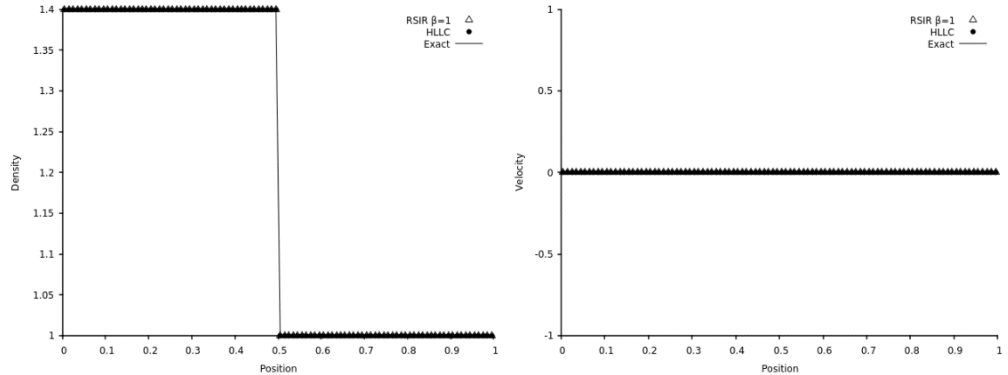


Figure II.9 – Test 5 of Toro (2009) page 334 (strong shock tube test of Test 3 with non-zero initial velocity. Comparison of the RSIR, HLLC and exact solutions. The computational domain involves 100 cells and the Godunov first-order scheme is used with CFL=0.9. Results are shown at time $t=0.012$. The initial discontinuity is located at $x_0 = 0.8$. Both methods show comparable accuracy.



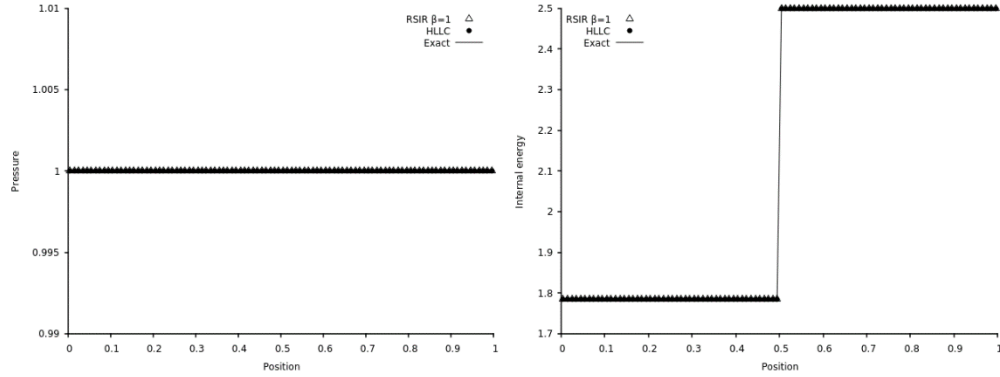


Figure II.10 – Test 6 of Toro (2009) page 334 (stationary contact discontinuity). Comparison of the RSIR, HLLC and exact solutions. The computational domain involves 100 cells and the Godunov first-order scheme is used with CFL=0.9. Results are shown at time $t=2$. The initial discontinuity is located at $x_0 = 0.5$. Both methods maintain stationary contact discontinuity.

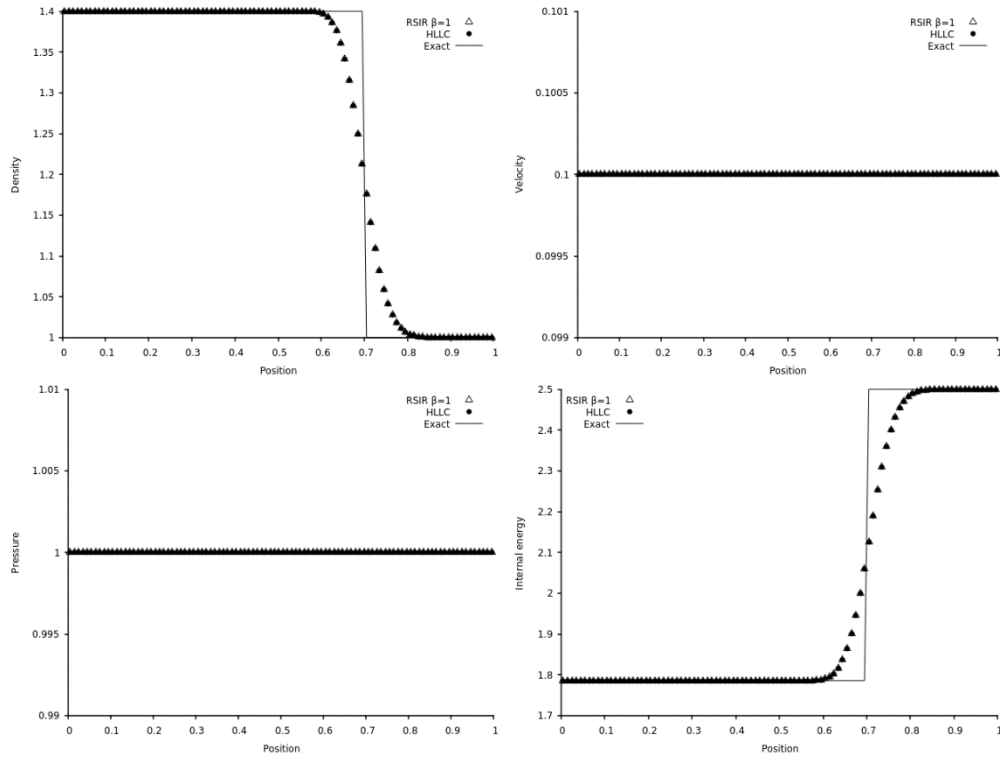


Figure II.11 – Test 7 of Toro (2009) page 334 (moving contact discontinuity). Comparison of the RSIR, HLLC and exact solutions. The computational domain involves 100 cells and the Godunov first-order scheme is used with CFL=0.9. Results are shown at time $t=2$. The initial discontinuity is located at $x_0 = 0.5$. Both methods show comparable accuracy.

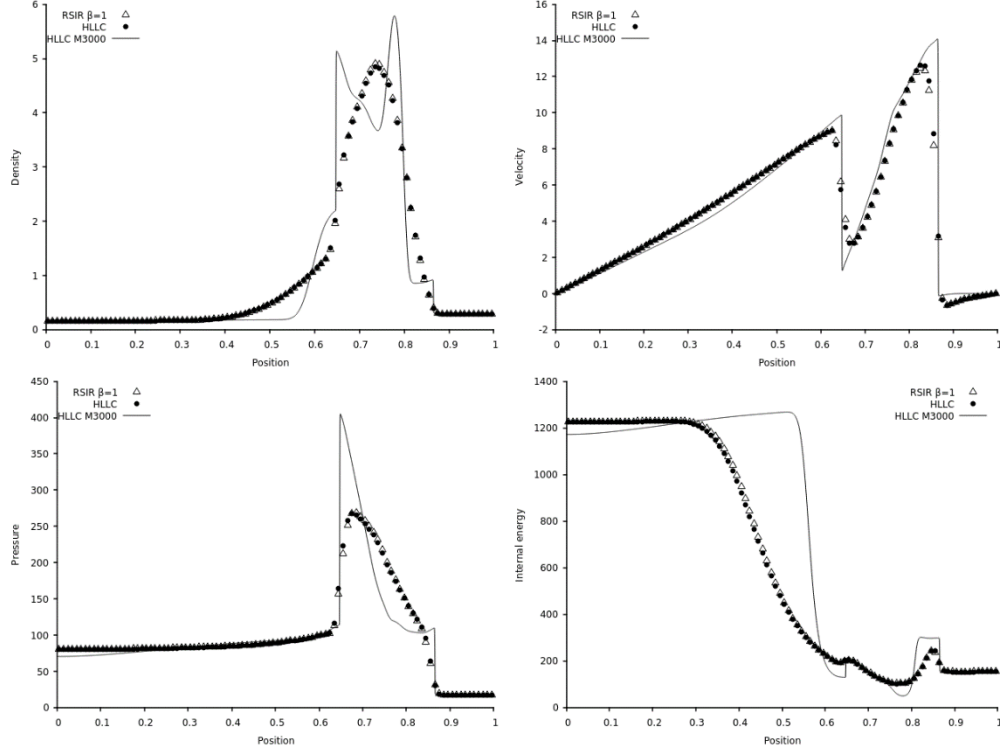


Figure II.12 – Woodward and Colella (1984) blast wave test (see also Toro 2009 page 612). Comparison of the RSIR and HLLC solutions. The computational domain involves 100 cells and the Godunov first-order scheme is used with CFL=0.9. Results are shown at time $t=0.038$. Both methods show comparable accuracy. This test problem has no exact solution, but computed results with the HLLC solver and 3000 cells are shown as reference solution.

The accuracy of the new solver is comparable to the one the HLLC solver, at least for the Euler equations and present test problems. HLLC appears more accurate in the double expansion test of Figure II.6 but this test is challenging as kinetic energy computation is problematic. Indeed, as in all computations based on conservative formulation of the Euler equations, the kinetic energy is computed from the cell average mass and momentum. However, at the center of the domain, the exact kinetic energy is different from the half square mean velocity.

Method's extension to the more sophisticated flow model of Saurel et al. (2017a) is now examined. As already mentioned, this system is weakly hyperbolic. Moreover, it will be shown that solutions are not self-similar.

III – Extension to dense-dilute two-phase flow model

The two-phase flow model of Saurel et al. (2017a), considering a dispersed phase 1 in a carrier fluid 2 is recalled hereafter. Pressure and velocity relaxation terms only are considered as interaction effects:

$$\begin{aligned} \frac{\partial \alpha_1}{\partial t} + \frac{\partial(\alpha u)}{\partial x} &= \mu(p_1 - p_2), \quad \mu \rightarrow +\infty \\ \frac{\partial(\alpha \rho)}{\partial t} + \frac{\partial(\alpha \rho u)}{\partial x} &= 0, \\ \frac{\partial(\alpha \rho u)}{\partial t} + \frac{\partial(\alpha \rho u^2 + \alpha p)}{\partial x} &= p_1 \frac{\partial \alpha_1}{\partial x} + \lambda(u_2 - u_1), \end{aligned}$$

$$\frac{\partial(\alpha\rho E)_1}{\partial t} + \frac{\partial(\alpha(\rho E + p)u)_1}{\partial x} = p_1 \frac{\partial(\alpha u)_1}{\partial x} + \lambda u_1(u_2 - u_1) - \mu p_1(p_1 - p_2), \quad (\text{III.1})$$

$$\frac{\partial(\alpha\rho)_2}{\partial t} + \frac{\partial(\alpha\rho u)_2}{\partial x} = 0,$$

$$\frac{\partial(\alpha\rho u)_2}{\partial t} + \frac{\partial(\alpha\rho u^2 + \alpha p)_2}{\partial x} = p_1 \frac{\partial\alpha_2}{\partial x} - \lambda(u_2 - u_1),$$

$$\frac{\partial(\alpha\rho E)_2}{\partial t} + \frac{\partial(\alpha(\rho E + p)u)_2}{\partial x} = -p_1 \frac{\partial(\alpha u)_1}{\partial x} - \lambda u_1(u_2 - u_1) + \mu p_1(p_1 - p_2).$$

Same notations as for the Euler equations are used. Additionally α_k represents the volume fraction of phase k , index I is related to interfacial variables and relaxation parameters are denoted by λ and μ , with respect to velocity and pressure relaxation. Appropriate relations are given for example in Saurel et al. (2017a). It is important to mention that this flow model is valid only in the stiff pressure relaxation limit ($\mu \rightarrow +\infty$). Appropriate pressure relaxation solvers are given for example in Lallemand and Saurel (2000). This is not equivalent to strict pressure equilibrium models that are non-hyperbolic, or conditionally hyperbolic. Also, this is not a restrictive assumption for most two-phase flow applications as pressure relaxation time is related to sound propagation in the dispersed phase, which is of the order of microseconds. Estimates for physical pressure relaxation times are given in Saurel et al. (2017a). Only specific situations, such as hot spots ignition in condensed energetic materials (Saurel et al., 2017b) require time resolution of the pressure relaxation process, as it is one of the driving effects for hot spot appearance. The present model is hyperbolic with wave speeds,

$$\lambda_{1-4} = u_1, \lambda_5 = u_2, \lambda_6 = u_2 - c_2 \text{ and } \lambda_7 = u_2 + c_2.$$

These wave speeds are the same as the ones of the Marble (1963) model but are significantly different from those of the BN model. Combination of the equations of System (III.1) results in the following mixture entropy equation, that guarantees non-negative evolutions,

$$\frac{\partial\alpha_1\rho_1s_1 + \alpha_2\rho_2s_2}{\partial t} + \frac{\partial\alpha_1\rho_1s_1u_1 + \alpha_2\rho_2s_2u_2}{\partial x} = \left(\frac{(u_1 - u_1)}{T_1} - \frac{(u_1 - u_2)}{T_2} \right) \lambda(u_2 - u_1). \quad (\text{III.2})$$

Indeed, admissible estimates for the interfacial velocity are,

$$u_I = u_1 \text{ or } u_I = u_2,$$

or combinations of them.

System (III.1) is obviously non-conservative, as $p_1 \frac{\partial\alpha_1}{\partial x}$ and $p_1 \frac{\partial(\alpha u)_1}{\partial x}$ terms are present in the right-

hand side of the momentum and energy equations. However, assuming $p_1 = p_1$ the following Rankine-Hugoniot system is obtained (Saurel et al., 2017a):

$$\begin{aligned} \alpha_1 &= \alpha_1^0, \\ \rho_1 &= \rho_1^0, \\ e_1 &= e_1^0, \\ u_1 &= u_1^0, \\ \rho_2(u_2 - \sigma) &= \rho_2^0(u^0 - \sigma), \\ \rho_2 u_2(u_2 - \sigma) + p_2 &= \rho_2^0 u^0(u^0 - \sigma) + p^0, \\ \rho_2 E_2(u_2 - \sigma) + u_2 p_2 &= \rho_2^0 E_2^0(u^0 - \sigma) + u^0 p^0. \end{aligned} \quad (\text{III.3})$$

These relations will be used in the RSIR derivation. As a consequence of (III.3), $p_1 = p_1^0$ meaning that pressure jump is absent in the dilute phase across shocks.

Numerical resolution of System (III.1) has been done in Saurel et al. (2017a) with the help of a Rusanov-type (1961) solver. This later being quite diffusive, the aim is now to build an improved solver. System (III.1) involves however three main difficulties:

- It is non-conservative;
- The eigenvalue u_1 is multiple. Therefore System (III.1) admits multivalued solutions (Forestier and Le Floch, 1992, Saurel et al., 1994, Bouchut et al., 2003).
- Solutions are not self-similar, as will be shown later with the help of numerical experiments.

These issues are addressed gradually in the following.

III.1 Local conservative formulation and Rusanov-type solvers

In Saurel et al. (2017a) a Rusanov-type method was derived to determine qualitative solutions of the new flow model and validations against both exact solutions and experimental data. This method is recalled hereafter, and an improved version based on a local conservative formulation is built. The aim is to show that non-conservative terms are treated correctly through the local conservative formulation.

a) Basic Rusanov version

System (III.1) is considered in non-conservative form and in the absence of relaxation terms as,

$$\frac{\partial \mathbf{U}}{\partial t} + \frac{\partial \mathbf{F}(\mathbf{U})}{\partial x} + \mathbf{H}\left(\mathbf{U}, \frac{\partial \mathbf{U}}{\partial x}\right) = 0, \quad (\text{III.4})$$

with,

$$\begin{aligned} \mathbf{U} &= (\alpha_1, (\alpha\rho)_1, (\alpha\rho u)_1, (\alpha\rho E)_1, (\alpha\rho)_2, (\alpha\rho u)_2, (\alpha\rho E)_2)^T, \\ \mathbf{F} &= ((\alpha u)_1, (\alpha\rho u)_1, (\alpha\rho u^2 + \alpha p)_1, (\alpha(\rho E + p)u)_1, (\alpha\rho u)_2, (\alpha\rho u^2 + \alpha p)_2, (\alpha(\rho E + p)u)_2)^T, \\ \mathbf{H} &= \left(0, 0, -p_1 \frac{\partial \alpha_1}{\partial x}, -p_1 \frac{\partial (\alpha u)_1}{\partial x}, 0, p_1 \frac{\partial \alpha_1}{\partial x}, p_1 \frac{\partial (\alpha u)_1}{\partial x}\right)^T. \end{aligned}$$

Let us denote by,

$$\mathbf{S} = \text{Max} \left\{ |u_{k,L}| + c_{k,L}, |u_{k,R}| + c_{k,R} \right\}, \quad k=1,2,$$

the maximum wave speed separating two states L and R. Note that the sound speed of the dispersed phase is considered in the extreme wave speed approximation only. This choice is likely to produce a more robust scheme. The Rusanov flux reads,

$$\mathbf{F}^* = \frac{1}{2} \left[\mathbf{F}_R + \mathbf{F}_L - \mathbf{S}(\mathbf{U}_R - \mathbf{U}_L) \right],$$

and the Godunov scheme associated to System (III.4) reads,

$$\mathbf{U}_i^{n+1} = \mathbf{U}_i^n - \frac{\Delta t}{\Delta x} \left(\mathbf{F}_{i+1/2}^* - \mathbf{F}_{i-1/2}^* \right) + \Delta t \mathbf{H}_i,$$

where H_i is an approximation of the non-conservative terms.

Following Saurel et al. (2017a), based on the method of Saurel and Abgrall (1999) for a slightly different flow model, approximation of these terms read;

- For the momentum equation,

$$H_{1,i,u} = p_{1,i}^n \frac{\alpha_{1,i+\frac{1}{2}}^* - \alpha_{1,i-\frac{1}{2}}^*}{\Delta x} \text{ with } \alpha_{1,i+\frac{1}{2}}^* = \frac{\alpha_{1,i} + \alpha_{1,i+1}}{2}.$$

- For the energy equations,

$$H_{1,i,E} = p_{1,i}^n \frac{(\alpha u)_{1,i+\frac{1}{2}}^* - (\alpha u)_{1,i-\frac{1}{2}}^*}{\Delta x} \text{ with } (\alpha u)_{1,i+\frac{1}{2}}^* = \frac{(\alpha u)_{1,i+1} + (\alpha u)_{1,i}}{2}.$$

These formulas are built to fulfill mechanical equilibrium condition. Another version is examined hereafter.

b) Local conservative formulation

The interfacial pressure p_1 appears in the non-conservative terms $p_1 \frac{\partial \alpha_k}{\partial x}$. As p_1 has been assumed equal to the pressure of the dispersed phase, the following assumption is made:

$$p_1 = \begin{cases} p_{1,L} & \text{if } \alpha_{1,L} > \alpha_{1,R}, \\ p_{1,R} & \text{if } \alpha_{1,L} < \alpha_{1,R}. \end{cases} \quad (\text{III.5})$$

It means that p_1 is taken equal to the pressure of phase 1 when this phase is present. Possible situations are schematized in Figure III.1.

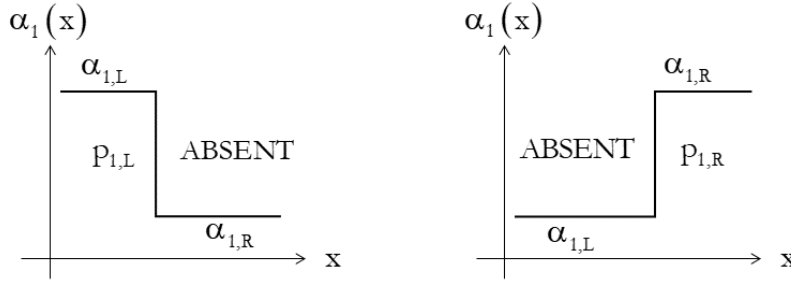


Figure III.1 – Schematic representation of the estimate for p_1 . As a consequence of jump conditions (III.3) both volume fraction and pressure of phase 1 are invariant across the right- and left-facing extreme waves in the RP solution.

Therefore, p_1 is taken equal to the pressure of phase 1 when this phase is present, as summarized in (III.5). As it is constant during time evolution in a given RP, it becomes a local constant.

As a consequence of Rankine-Hugoniot relations (III.3), assuming $p_1 = p_1$ and considering (III.5), p_1 becomes a local constant, as p_1 is invariant across extreme right- and left-facing waves.

Thanks to this local constant, System (III.4) becomes locally conservative:

$$\begin{aligned} \frac{\partial \alpha_1}{\partial t} + \frac{\partial (\alpha u)_1}{\partial x} &= 0, \\ \frac{\partial (\alpha \rho)_1}{\partial t} + \frac{\partial (\alpha \rho u)_1}{\partial x} &= 0, \\ \frac{\partial (\alpha \rho u)_1}{\partial t} + \frac{\partial (\alpha \rho u^2 + \alpha (p - p_1))_1}{\partial x} &= 0, \\ \frac{\partial (\alpha \rho E)_1}{\partial t} + \frac{\partial (\alpha (\rho E + p - p_1) u)_1}{\partial x} &= 0, \end{aligned} \quad (\text{III.6})$$

$$\begin{aligned}\frac{\partial \alpha_2}{\partial t} - \frac{\partial(\alpha_1 u_1)}{\partial x} &= 0, \\ \frac{\partial(\alpha \rho)_2}{\partial t} + \frac{\partial(\alpha \rho u)_2}{\partial x} &= 0, \\ \frac{\partial(\alpha \rho u)_2}{\partial t} + \frac{\partial(\alpha \rho u^2 + \alpha(p - p_I))_2}{\partial x} &= 0, \\ \frac{\partial(\alpha \rho E)_2}{\partial t} + \frac{\partial(\alpha(\rho E + p)u)_2}{\partial x} + (\alpha u)_1 p_I &= 0.\end{aligned}$$

In compact form it reads,

$$\frac{\partial \mathbf{U}}{\partial t} + \frac{\partial \Phi(\mathbf{U})}{\partial x} = 0,$$

with obvious definition for $\Phi(\mathbf{U})$.

The associated Rusanov fluxes are immediate,

$$\Phi^* = \frac{1}{2} [\Phi_R + \Phi_L - S(U_R - U_L)]. \quad (\text{III.7})$$

From Φ^* , the \mathbf{F}^* fluxes of formulation (III.4) are deduced as,

$$\mathbf{F}_k^* = \Phi_k^* + p_I \begin{pmatrix} 0 \\ 0 \\ \alpha_k^* \\ \Phi^*(\alpha_k) \end{pmatrix}, \quad k=1,2. \quad (\text{III.8})$$

α_k^* are determined from the Rusanov state as,

$$\alpha_k^* = \frac{1}{2} \left[\alpha_{k,R} + \alpha_{k,L} - \frac{(\Phi(\alpha_{k,R}) - \Phi(\alpha_{k,L}))}{S} \right]. \quad (\text{III.9})$$

The fluxes are inserted in the same Godunov scheme as before,

$$\mathbf{U}_i^{n+1} = \mathbf{U}_i^n - \frac{\Delta t}{\Delta x} (\mathbf{F}_{i+1/2}^* - \mathbf{F}_{i-1/2}^*) + \Delta t \mathbf{H}_i,$$

except that \mathbf{H}_i are now given by,

$$\begin{aligned} \mathbf{H}_{i,u} &= p_i^n \frac{\alpha_{1,i+1/2}^* - \alpha_{1,i-1/2}^*}{\Delta x}, \\ \mathbf{H}_{i,E} &= p_i^n \frac{\Phi_{1,i+1/2}^*(\alpha_1) - \Phi_{1,i-1/2}^*(\alpha_1)}{\Delta x}. \end{aligned}$$

In these expressions $\alpha_{k,i\pm\frac{1}{2}}^*$ and $\Phi_{1,i\pm\frac{1}{2}}^*(\alpha_1)$ are given by (III.9) and (III.7) respectively.

The overall scheme is consequently quite different from the basic version presented before.

The two Rusanov solvers are now compared on an arbitrary shock tube test problem, in the absence of velocity relaxation, but with stiff pressure relaxation. Corresponding results are shown in Figure III.2.

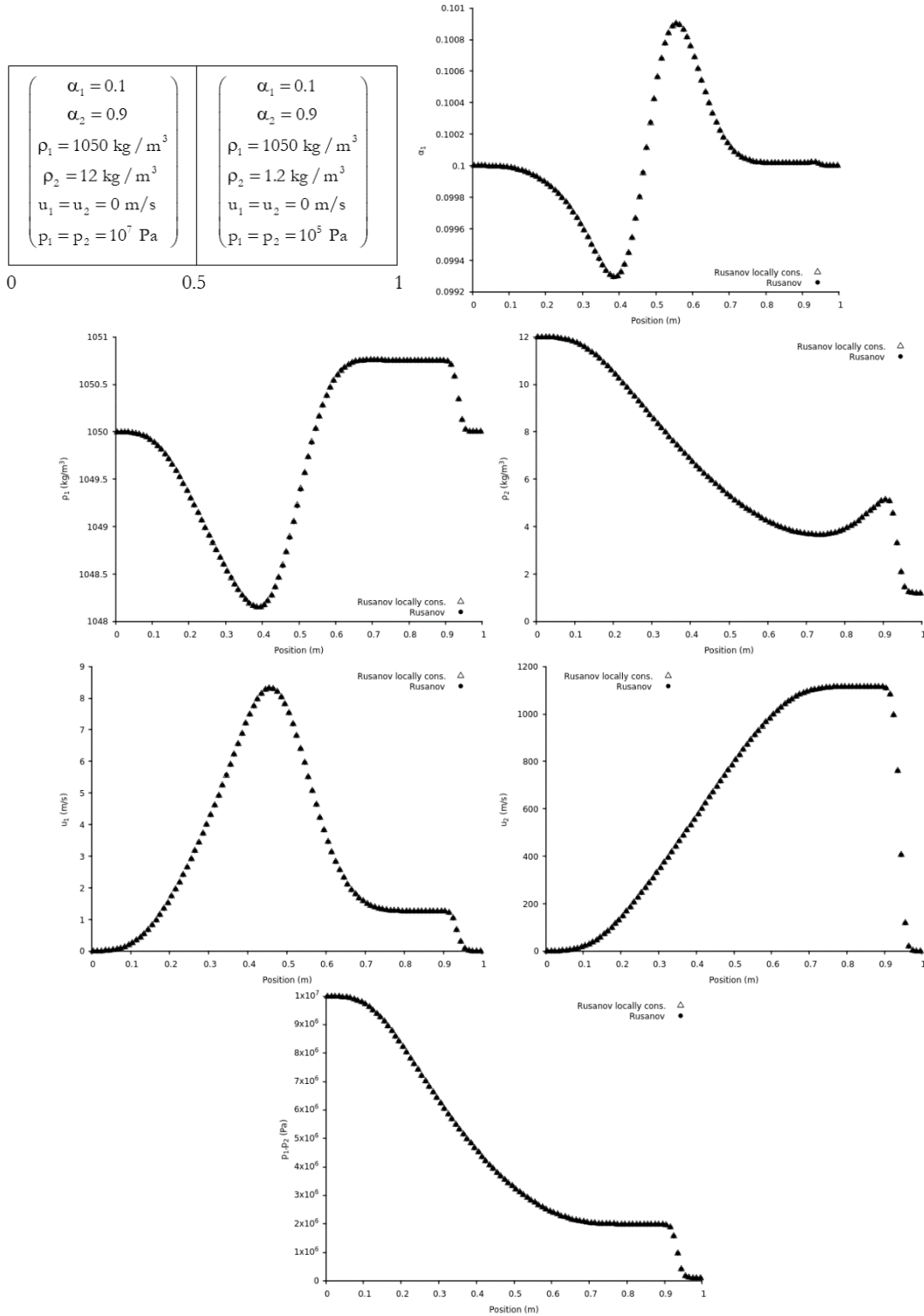


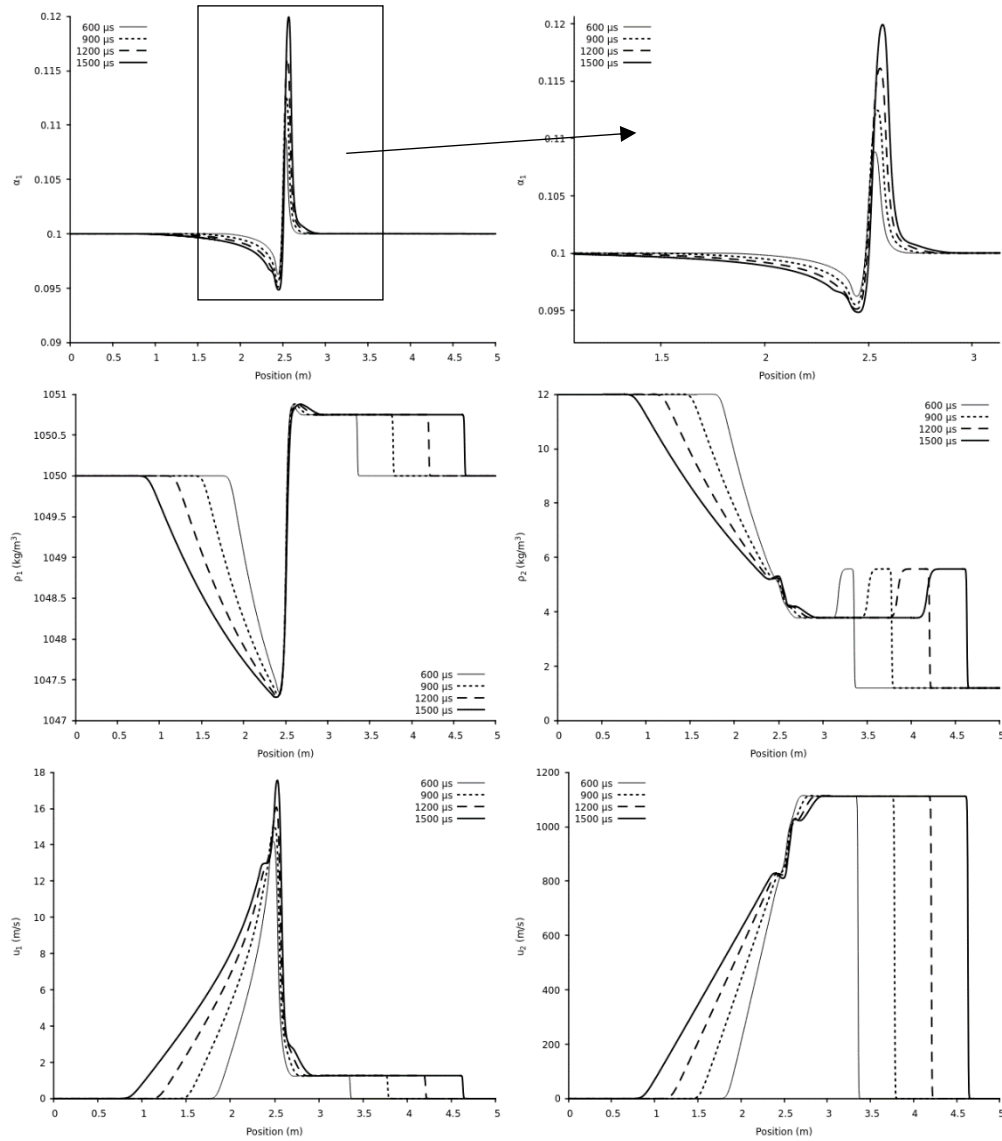
Figure III.2 – Comparison of the two Rusanov solvers on a two-phase shock tube test. Phase 1 corresponds to the dispersed fluid, considered here as liquid water, with SG EOS parameters ($\gamma_1 = 4.4$ and $p_{\infty 1} = 6 \cdot 10^8 \text{ Pa}$). Phase 2

represents the carrier phase, here air considered as ideal gas ($\gamma_2 = 1.4$). Stiff pressure relaxation is used at any time. The computational domain involves 100 cells and the Godunov first-order scheme is used with CFL=0.9. Results are shown at $t=300 \mu\text{s}$. Both results are perfectly merged validating the approach based on the local conservative formulation.

Extra tests have been carried out, such as double expansion and double shock tests, always showing the same agreement. The local conservative formulation (III.6) with local constant (III.5) is consequently robust enough to be considered with the reconstruction method (RSIR).

c) Non self-similar solutions

Another difficulty is highlighted hereafter. The same shock tube test case as before is reconsidered and the solution is shown at various times in Figure III.3.



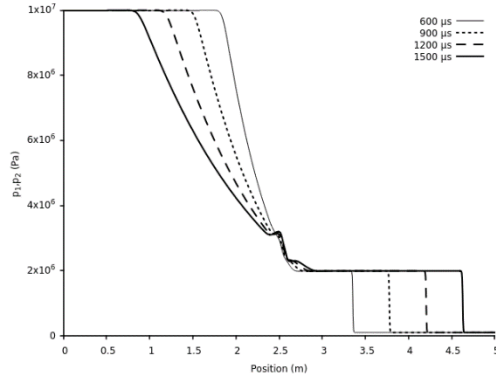
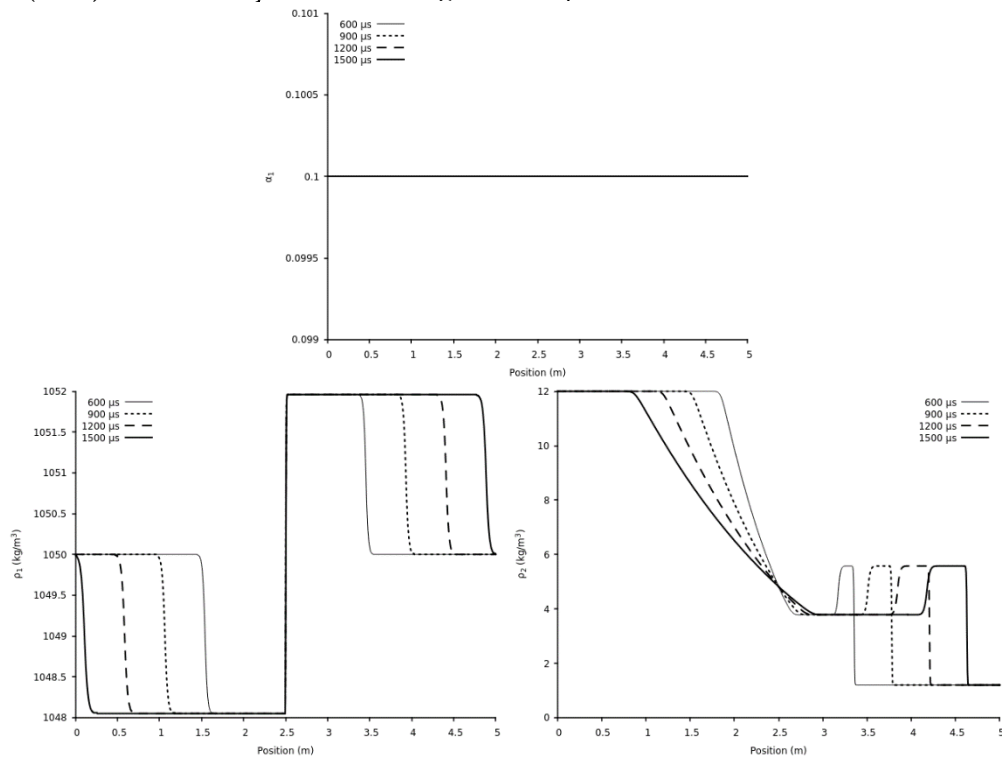


Figure III.3 – Shock tube test problem of Figure III.2 considered at various times. Length of the domain has been increased to 5 m to avoid wave interaction with the boundaries, and the initial discontinuity is placed at 2.5 m. Stiff pressure relaxation is used at any time. 1 000 computational cells are used with CFL=0.5. Computations are done with the MUSCL method and Minmod limiter. Profiles for the carrier phase (2) appear quite self-similar but profiles of the dilute phase (1) are not, regarding volume fraction and velocity. Volume fraction of the dilute phase keeps increasing without converging towards a constant state. The same tendency is observed in the velocity plot of the dilute phase. These observations are mesh and solver independent.

Origin of this interesting behavior is examined hereafter with the help of the BN model. The same shock tube test problem is rerun with this model with the help of the HLLC-type solver of Furfaro and Saurel (2015). In the computations of Figure III.4 pressure relaxation is absent.



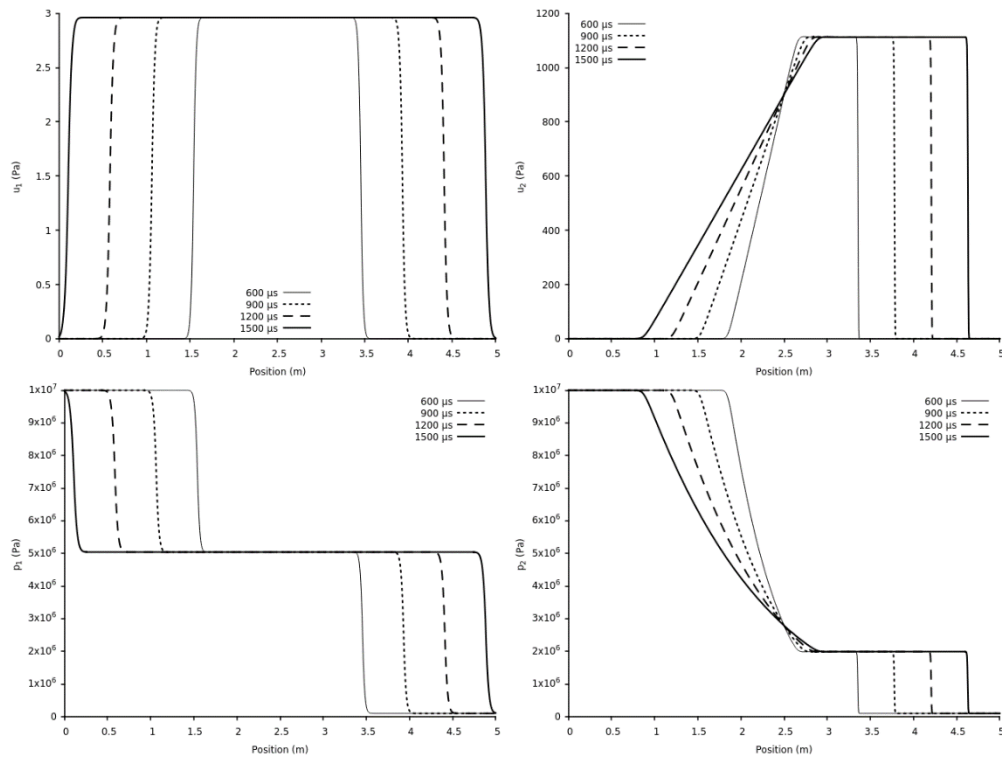
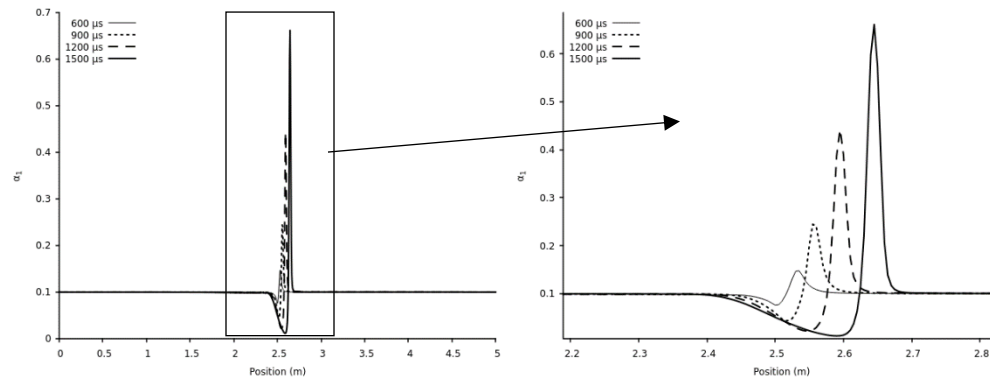


Figure III.4 – Two-phase shock tube problem of Figure III.2 computed with the BN model in the absence of pressure relaxation. Length of the domain has been increased to 5 m to avoid wave interaction with the boundaries, and the initial discontinuity is placed at 2.5 m. 1 000 computational cells are used with CFL=0.5. Computations are done with the MUSCL method and Minmod limiter. The solution is self-similar and consists in two decoupled shock tube solutions, as well known.

The same shock tube test problem is reconsidered once more with stiff pressure relaxation in the BN model. Corresponding results are shown in Figure III.5.



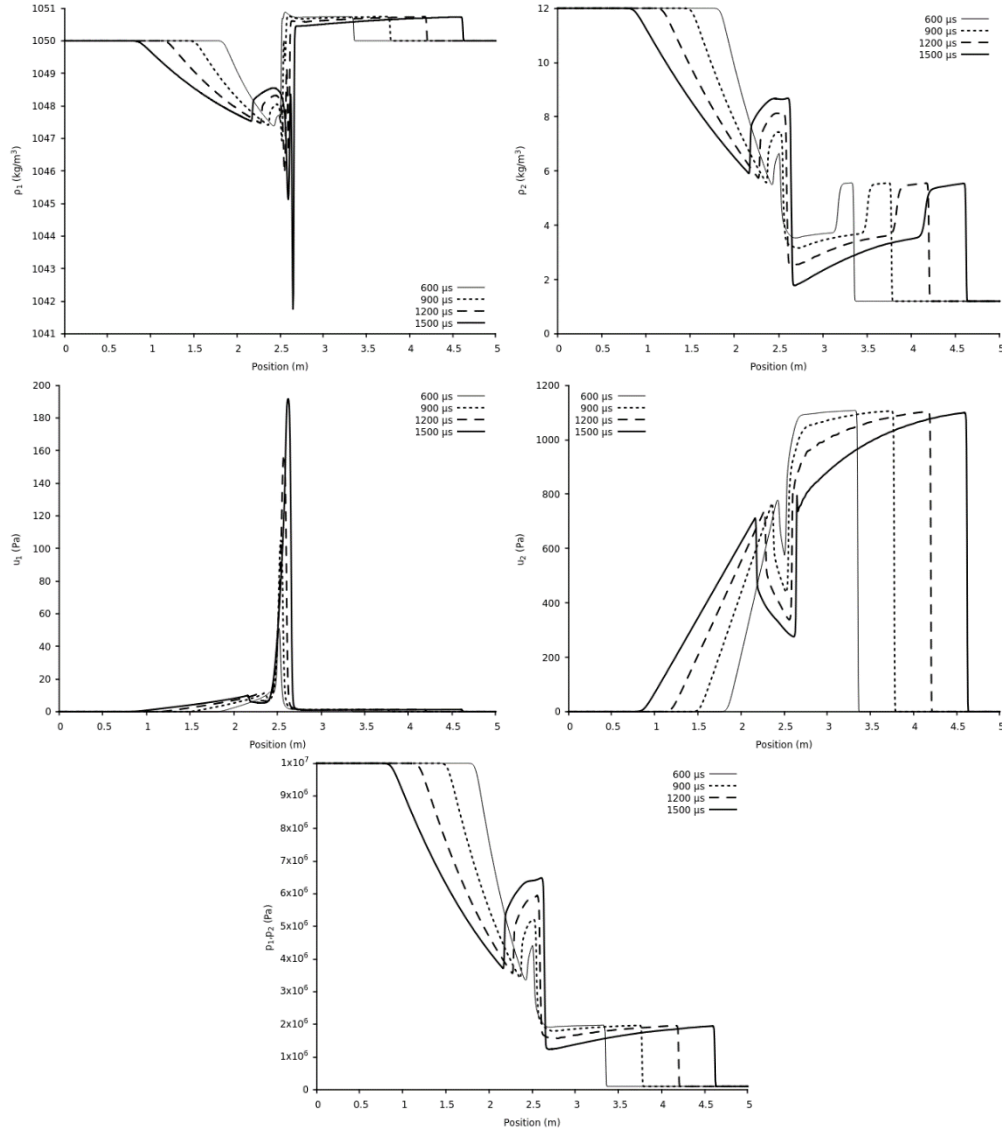


Figure III.5 – Two-phase shock tube problem of Figure III.2 computed with the BN model with stiff pressure relaxation. Length of the domain has been increased to 5 m to avoid wave interaction with the boundaries, and the initial discontinuity is placed at 2.5 m. 1 000 computational cells are used with CFL=0.5. Computations are done with the MUSCL method and Minmod limiter. The solution is not self-similar. This is not surprising as source terms related to pressure relaxation are present.

When stiff pressure relaxation is considered, solutions of the BN model are no longer self-similar, and this is not surprising. It explains why solutions of flow model (III.1) are not self-similar, as this flow model only has sense in the stiff pressure relaxation limit. It thus appears that stiff pressure relaxation induces volume fraction gradients that in turn activate non-conservative terms in the momentum equations, acting as a drag force, in differential form. This drag force increases as volume fraction gradient increases as well.

Another interesting feature appears with solutions of Figures III.3 and III.5. Solution for the velocity of the dispersed phase appears multivalued, as schematized in Figure III.6. The left and right star velocities are different, implying particle clustering, with a Dirac type volume fraction profile. Such behavior also appears with the BN model (Figure III.5) as a combination of pressure relaxation and non-conservative terms.

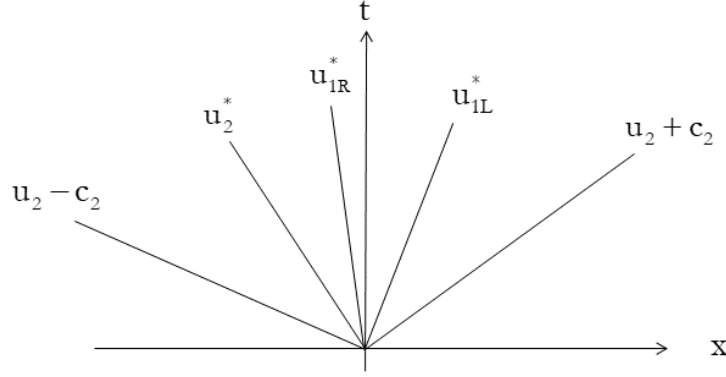


Figure III.6 – Schematic representation of the multivalued phase 1 velocity. Differences in the right and left star velocities of the dispersed phase may result in particle clustering as time evolves. This effect is present in the computations of Figures III.3 and III.5.

This particle clustering effect appears in former one-dimensional computations as a result of pressure relaxation effects that create volume fraction gradients. As soon as the volume fraction is not uniform, non-conservative terms activate and induce drag effects among the phases. As time evolves, particle clustering appears. This effect seems a possible mechanism for the fingering instability studied in Section IV.

Extension of the RSIR method is now addressed for this non-trivial flow model.

III.2 Riemann solver with internal reconstruction (RSIR) for the two-phase model

The present flow solver is not based on variations across the various waves but only on rebuilding two intermediate states to preserve isolated volume fraction discontinuities and reduce artificial smearing during transport. In this direction, the intermediate wave speed corresponds to the contact wave of phase 1 (dispersed phase):

$$S_{M,1} = \frac{U_{HLL}^* \left((\alpha \rho u)_1 \right)}{U_{HLL}^* \left((\alpha \rho)_1 \right)}, \quad (III.10)$$

with U_{HLL}^* given by (III.11) for System (III.6). The extreme wave speeds are approximated through Davis (1988) as,

$$S_L = \text{Min} \left\{ u_{k,L} - c_{k,L}, u_{k,R} - c_{k,R} \right\}, \quad k=1,2.$$

$$S_R = \text{Max} \left\{ u_{k,L} + c_{k,L}, u_{k,R} + c_{k,R} \right\},$$

As detailed with the Euler equations, the method to solve System (III.1) proceeds in two steps:

- Determine an average state with HLL based on (III.6);
- Rebuild the solution.

Thanks to the local conservative formulation the first step is immediate. System (III.6) is expressed as,

$$\frac{\partial U}{\partial t} + \frac{\partial \Phi(U)}{\partial x} = 0,$$

with p_i given by (III.5).

The average state is obtained as,

$$U_{HLL}^* = \frac{\Phi_R - \Phi_L + S_L U_L - S_R U_R}{S_L - S_R}. \quad (III.11)$$

The next step consists in the approximation of states \mathbf{L}^* and \mathbf{R}^* . Knowledge of the intermediate wave speed $S_{M,1}$ from (III.10) enables the following decomposition of the average state,

$$\mathbf{U}_{HLL}^* = \omega_R \mathbf{U}_R^* + \omega_L \mathbf{U}_L^*, \quad (\text{III.12})$$

with,

$$\omega_R = \frac{S_R - S_{M,1}}{S_R - S_L} \quad \text{and} \quad \omega_L = \frac{S_{M,1} - S_L}{S_R - S_L}.$$

As System (III.12) involves two unknown variable vectors, another set of relations is needed.

Reconstruction of the dispersed phase

For the dispersed phase, the Rankine-Hugoniot relations (III.3) imply, $\alpha_{1,R}^* = \alpha_{1,R}$ and $\alpha_{1,L}^* = \alpha_{1,L}$.

The difference of these two relations reads,

$$\alpha_{1,R}^* - \alpha_{1,L}^* = \alpha_{1,R} - \alpha_{1,L}.$$

As before with the Euler equations, parameter β is introduced for the sake of generality only,

$$\alpha_{1,R}^* - \alpha_{1,L}^* = \beta (\alpha_{1,R} - \alpha_{1,L}) = \Psi_{\alpha_1}. \quad (\text{III.13})$$

However, either $\beta = 0$ (HLL) or $\beta = 1$ (alternative to HLLC) is to be considered. Extra information regarding parameter β will be provided further with the analysis of a specific configuration.

As the density of phase 1 has no jump across the left- and right-facing waves, a similar relation is obtained:

$$(\alpha\rho)_{1,R}^* - (\alpha\rho)_{1,L}^* = \beta ((\alpha\rho)_{1,R} - (\alpha\rho)_{1,L}) = \Psi_{1,\text{mass}}. \quad (\text{III.14})$$

Regarding the momentum jump across the intermediate wave, the following relation is introduced, as done for the Euler equations,

$$(\alpha\rho\mathbf{u})_{1,R}^* - (\alpha\rho\mathbf{u})_{1,L}^* = \beta ((\alpha\rho)_{1,R} - (\alpha\rho)_{1,L}) \mathbf{S}_{M,1} = \Psi_{1,\text{momentum}}. \quad (\text{III.15})$$

The energy jump is now addressed with the help one more time of the Rankine-Hugoniot relations (III.3) of the dispersed phase, expressing invariance of densities and pressures across the extreme waves S_L and S_R . With the help of the EOS it yields,

$$\mathbf{E}_{1,L}^* = \mathbf{e}_{1,L}^*(p_{1,L}, \rho_{1,L}) + \frac{1}{2} \mathbf{S}_{M,1}^2,$$

$$\mathbf{E}_{1,R}^* = \mathbf{e}_{1,R}^*(p_{1,R}, \rho_{1,R}) + \frac{1}{2} \mathbf{S}_{M,1}^2.$$

The energy jump across wave $\mathbf{S}_{M,1}$ consequently reads,

$$(\alpha\rho\mathbf{E})_{1,R}^* - (\alpha\rho\mathbf{E})_{1,L}^* = \beta ((\alpha\rho)_{1,R} \mathbf{E}_{1,R}^* - (\alpha\rho)_{1,L} \mathbf{E}_{1,L}^*) = \Psi_{1,\text{energy}}, \quad (\text{III.16})$$

where the parameter β is introduced for the same reasons as before.

The previous relations summarize as,

$$\mathbf{U}_{1,R}^* = \mathbf{U}_{1,L}^* + \Psi_1, \quad (\text{III.17})$$

where $\Psi_1 = (\Psi_{\alpha_1}, \Psi_{1,\text{mass}}, \Psi_{1,\text{momentum}}, \Psi_{1,\text{energy}})^T$, with components given in (III.13-15).

Combining (III.12) and (III.17) the intermediate states are finally computed as,

$$\begin{cases} \mathbf{U}_{1,R}^* = \mathbf{U}_{1,HLL}^* + \omega_L \Psi_1, \\ \mathbf{U}_{1,L}^* = \mathbf{U}_{1,HLL}^* - \omega_R \Psi_1. \end{cases} \quad (\text{III.18})$$

Reconstruction of the carrier phase

The second phase is now addressed. Thanks to the previous treatment of the dispersed phase and the saturation condition, the determination of the volume fractions is immediate,

$$\begin{aligned} \alpha_{L,2}^* &= 1 - \alpha_{L,1}^*, \\ \alpha_{R,2}^* &= 1 - \alpha_{R,1}^*. \end{aligned} \quad (\text{III.19})$$

This result is directly used in the following. Note that the preceding relations can be rewritten as,

$$\alpha_{2,R}^* - \alpha_{2,L}^* = \beta (\alpha_{2,R} - \alpha_{2,L}) = \Psi_{\alpha_2},$$

to preserve compatibility with (III.13).

The contact wave speed of the second phase is computed as,

$$S_{M2} = \frac{U_{HLL}^* ((\alpha \rho u)_2)}{U_{HLL}^* ((\alpha \rho)_2)}.$$

At this level no distinction is made between the left and right velocities of the carrier phase: $u_{2,L}^* = u_{2,R}^* = S_{M,2}$. Similarly to the RSIR solver developed for the Euler equations, the thermodynamic evolutions through the right- and left-facing waves are approximated as isentropic. The isentropic evolutions are themselves approximated through sound speed definition and trapezoidal approximation as,

$$\bar{c}_2^2 = \frac{p_{2,R}^* - p_{2,R}}{\rho_{2,R}^* - \rho_{2,R}}, \quad (\text{III.20})$$

$$\bar{c}_2^2 = \frac{p_{2,L}^* - p_{2,L}}{\rho_{2,L}^* - \rho_{2,L}},$$

where,

$$\bar{c}_2 = \frac{1}{2} (c_{2,L} + c_{2,R}).$$

System (III.20) becomes,

$$p_{2,R}^* = p_{2,R} + \bar{c}_2^2 (\rho_{2,R}^* - \rho_{2,R}), \quad (\text{III.21})$$

$$p_{2,L}^* = p_{2,L} + \bar{c}_2^2 (\rho_{2,L}^* - \rho_{2,L}).$$

The Rankine-Hugoniot relation of the momentum equation of phase 2, in locally conservative form, is now considered across the intermediate wave $S_{M,1}$,

$$(\alpha \rho)_{2,R}^* S_{M,2} (S_{M,2} - S_{M,1}) + \alpha_{2,R}^* (p_{2,R}^* - p_I) = (\alpha \rho)_{2,L}^* S_{M,2} (S_{M,2} - S_{M,1}) + \alpha_{2,L}^* (p_{2,L}^* - p_I). \quad (\text{III.22})$$

Combining (III.21) and (III.22) results in,

$$(\alpha \rho)_{R,2}^* - (\alpha \rho)_{L,2}^* = \beta \left(\frac{\alpha_{L,2}^* (p_{L,2} - p_I - \bar{c}_2^2 \rho_{L,2}) - \alpha_{R,2}^* (p_{R,2} - p_I - \bar{c}_2^2 \rho_{R,2})}{\bar{c}_2^2 + S_{M,2} (S_{M,2} - S_{M,1})} \right) = \Psi_{2,\text{mass}}, \quad (\text{III.23})$$

where parameter β is introduced as before. Relation (III.23) also yields the momentum jump,

$$(\alpha\rho\mathbf{u})_{R,2}^* - (\alpha\rho\mathbf{u})_{L,2}^* = \beta \left(\frac{\alpha_{L,2}^* (\mathbf{p}_{L,2} - \mathbf{p}_I - \bar{c}_2^2 \rho_{L,2}) - \alpha_{R,2}^* (\mathbf{p}_{R,2} - \mathbf{p}_I - \bar{c}_2^2 \rho_{R,2})}{\bar{c}_2^2 + \mathbf{S}_{M,2} (\mathbf{S}_{M,2} - \mathbf{S}_{M,1})} \right) \mathbf{S}_{M,2} = \Psi_{2,\text{momentum}}, \quad (\text{III.24})$$

as done in the context of the Euler equations.

The Rankine-Hugoniot relation of the momentum equation of phase 2, in locally conservative form, is now considered across the intermediate wave $\mathbf{S}_{M,2}$. In the present solver a single velocity is considered in the star state for each phase, and in particular for the second one $\mathbf{u}_{2,L}^* = \mathbf{u}_{2,R}^* = \mathbf{S}_{M,2}$. Consequently, the Rankine-Hugoniot relation of the momentum equation of phase 2 reduces to:

$$\alpha_{2,R}^* (\mathbf{p}_{2R}^* - \mathbf{p}_I) = \alpha_{2,L}^* (\mathbf{p}_{2L}^* - \mathbf{p}_I).$$

As the volume fraction varies only across the $\mathbf{S}_{M,1}$ wave, the last relation reduces to: $\mathbf{p}_{2R}^* = \mathbf{p}_{2L}^*$.

The star pressure for the second phase is consequently approximated by summing the two relations (III.21):

$$p_2^* = \frac{p_{L,2} + p_{R,2}}{2} + \bar{c}^2 \left(\frac{\rho_{L,2}^* + \rho_{R,2}^*}{2} - \frac{\rho_{L,2} + \rho_{R,2}}{2} \right).$$

This star pressure is assumed constant in all star states and in particular across the intermediate wave $\mathbf{S}_{M,1}$. Thanks to previous approximations and EOS of the second phase, the energy jump across wave $\mathbf{S}_{M,1}$ is determined as,

$$(\alpha\rho E)_{R,2}^* - (\alpha\rho E)_{L,2}^* = (\alpha\rho)_{R,2}^* \left(e(\mathbf{p}_2^*, \rho_{R,2}^*) + \frac{1}{2} \mathbf{S}_{M,2}^2 \right) - (\alpha\rho)_{L,2}^* \left(e(\mathbf{p}_2^*, \rho_{L,2}^*) + \frac{1}{2} \mathbf{S}_{M,2}^2 \right) = \Psi_{2,\text{energy}}. \quad (\text{III.25})$$

In this last relation parameter β is present in $(\alpha\rho)_{L,R,2}^*$.

The apparent densities in the star states are computed as,

$$\begin{cases} (\alpha\rho)_{L,2}^* = (\alpha\rho)_{\text{HLL},2}^* - \omega_R \Psi_{2,\text{mass}}, \\ (\alpha\rho)_{R,2}^* = (\alpha\rho)_{\text{HLL},2}^* + \omega_L \Psi_{2,\text{mass}}. \end{cases}$$

In compact form states of the carrier phase are computed as,

$$\begin{cases} \mathbf{U}_{2,L}^* = \mathbf{U}_{2,\text{HLL}}^* - \omega_R \Psi_2, \\ \mathbf{U}_{2,R}^* = \mathbf{U}_{2,\text{HLL}}^* + \omega_L \Psi_2, \end{cases} \quad (\text{III.26})$$

where $\Psi_2 = \left(\Psi_{\alpha_2}, \Psi_{2,\text{mass}}, \Psi_{2,\text{momentum}}, \Psi_{2,\text{energy}} \right)^T$, with components given in (III.19), (III.23), (III.24) and (III.25).

At this level, state vectors \mathbf{U}_R^* and \mathbf{U}_L^* are fully determined. Note that the RSIR solver does not depend on the form of the EOS.

Restrictions on parameter β

In the frame of the Euler equations, β belongs to the interval $0 \leq \beta \leq 1$, the minimum numerical dissipation corresponding to $\beta = 1$ as already mentioned.

When dealing with the present two-phase flow model two values only are admissible, $\beta = 0$ corresponding to the HLL version and $\beta = 1$ leading to the RSIR version with lowest dissipation.

This restriction can be understood with the following example of flow in mechanical equilibrium, where $\mathbf{p}_L = \mathbf{p}_R = \mathbf{p}_I = \mathbf{p} = \text{cst}$ and $\mathbf{S}_{M,1} = \mathbf{S}_{M,2} = \mathbf{u} = \text{cst}$.

Volume fraction and mass jump relations reduce in this situation to,

$$\alpha_{2,R}^* - \alpha_{2,L}^* = \beta(\alpha_{2,R} - \alpha_{2,L}) = \Psi_{\alpha_2},$$

$$(\alpha\rho)_{R,2}^* - (\alpha\rho)_{L,2}^* = \beta(\alpha_{R,2}^*\rho_{R,2} - \alpha_{L,2}^*\rho_{L,2}) = \Psi_{2,\text{mass}}.$$

The HLL solution (III.11) in this specific context reads for these two variables,

$$\alpha_{2,\text{HLL}}^* = \frac{(\mathbf{S}_L - \mathbf{u})\alpha_{2,L} - (\mathbf{S}_R - \mathbf{u})\alpha_{2,R}}{\mathbf{S}_L - \mathbf{S}_R},$$

$$(\alpha\rho)_{2,\text{HLL}}^* = \frac{(\mathbf{S}_L - \mathbf{u})(\alpha\rho)_{2,L} - (\mathbf{S}_R - \mathbf{u})(\alpha\rho)_{2,R}}{\mathbf{S}_L - \mathbf{S}_R}.$$

Using (III.26) the left intermediate state is determined as,

$$\alpha_{2,L}^* = \frac{((\mathbf{S}_L - \beta\mathbf{S}_R) + (\beta - 1)\mathbf{u})\alpha_{2,L} + ((\mathbf{S}_R - \mathbf{u})(\beta - 1)\alpha_{2,R})}{\mathbf{S}_L - \mathbf{S}_R},$$

$$(\alpha\rho)_{2,L}^* = \frac{((\mathbf{S}_L - \beta\mathbf{S}_R) + (\beta - 1)\mathbf{u})(\alpha\rho)_{2,L} + ((\mathbf{S}_R - \mathbf{u})(\beta - 1)(\alpha\rho)_{2,R})}{\mathbf{S}_L - \mathbf{S}_R}.$$

Similar expressions are obtained for the right state.

Consequently, the star density of phase 2 reads,

$$\rho_{2,L}^* = \frac{((\mathbf{S}_L - \beta\mathbf{S}_R) + (\beta - 1)\mathbf{u})(\alpha\rho)_{2,L} + ((\mathbf{S}_R - \mathbf{u})(\beta - 1)(\alpha\rho)_{2,R})}{((\mathbf{S}_L - \beta\mathbf{S}_R) + (\beta - 1)\mathbf{u})\alpha_{2,L} + ((\mathbf{S}_R - \mathbf{u})(\beta - 1)\alpha_{2,R})}. \quad (\text{III.27})$$

Using (III.21) the star pressure in the left state is given by,

$$p_{2,L}^* = p_{2,L} + \bar{c}_2^2(\rho_{2,L}^* - \rho_{2,L}).$$

To maintain mechanical equilibrium the following condition is mandatory: $p_{2,L}^* = p_{2,L}$.

Such condition is satisfied only if $\rho_{2,L}^* = \rho_{2,L}$. Relation (III.27) fulfills this requirement only when $\beta = 1$.

Numerical fluxes and time evolution

Local conservative fluxes are computed as,

$$\begin{cases} \Phi_R^* = \Phi_R + \mathbf{S}_R (\mathbf{U}_R^* - \mathbf{U}_R), \\ \Phi_L^* = \Phi_L + \mathbf{S}_L (\mathbf{U}_L^* - \mathbf{U}_L). \end{cases} \quad (\text{III.28})$$

Fluxes of System (III.1) are computed as,

$$\mathbf{F}_k^* = \Phi_k^* + \Lambda_k \quad k = \mathbf{L}, \mathbf{R}, \quad (\text{III.29})$$

with $\Lambda_k = p_1 \left(0, \quad 0, \quad \alpha_{1k}^*, \quad (\alpha\mathbf{u})_{1k}^*, \quad 0, \quad (1 - \alpha_{1k}^*), \quad -(\alpha\mathbf{u})_{1k}^* \right)^T$.

α_{1k}^* are determined from the reconstructed states as,

$$\begin{cases} \alpha_{1L}^* = \alpha_{1\text{HLL}}^* - \omega_R \beta (\alpha_{1R} - \alpha_{1L}), \\ \alpha_{1R}^* = \alpha_{1\text{HLL}}^* + \omega_L \beta (\alpha_{1R} - \alpha_{1L}). \end{cases} \quad (\text{III.30})$$

The associated Godunov-type scheme including non-conservative terms reads,

$$\mathbf{U}_i^{n+1} = \mathbf{U}_i^n - \frac{\Delta t}{\Delta X} \left(\mathbf{F}_{i+1/2}^* - \mathbf{F}_{i-1/2}^* \right) + \Delta t \mathbf{H}_i, \quad (\text{III.31})$$

with H_i given by,

$$H_{i,u} = p_i^n \frac{\alpha_{1,i+1/2}^* - \alpha_{1,i-1/2}^*}{\Delta x},$$

$$H_{i,E} = p_i^n \frac{\Phi_{i+1/2}^*(\alpha_1) - \Phi_{i-1/2}^*(\alpha_1)}{\Delta x}.$$

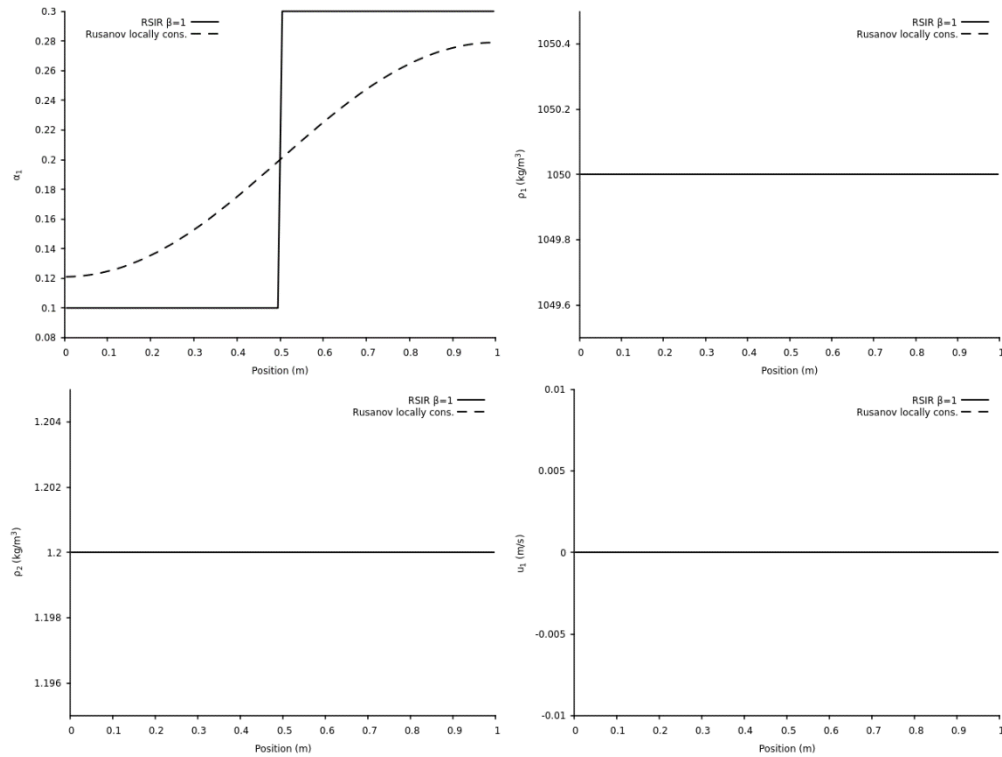
In these expressions $\alpha_{k,i\pm 1/2}^*$ and $\Phi_{i\pm 1/2}^*(\alpha_1)$ are deduced from (III.30) and (III.28) respectively.

III.3 Examples and validations

Validations of the flow solver and comparisons with the former Rusanov method are addressed first. Second computational examples are considered showing method's capabilities.

a) Validation of the RSIR solver

A volume fraction discontinuity at rest is considered to check method's capability to maintain such stationary wave. Corresponding results are shown in Figure III.7.



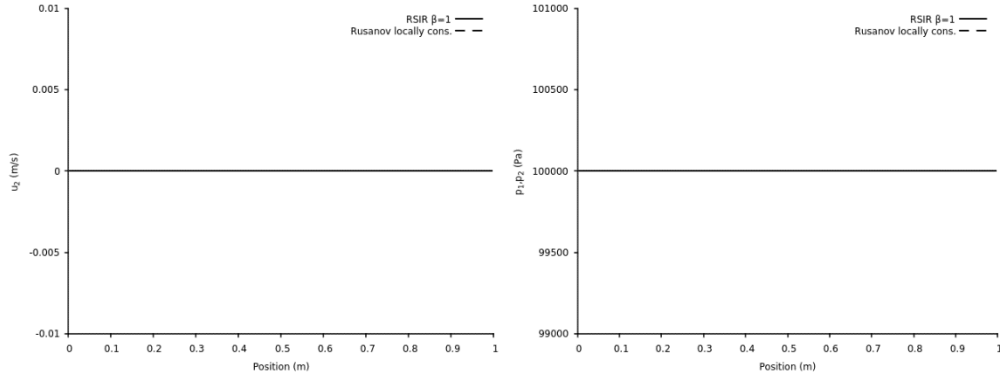
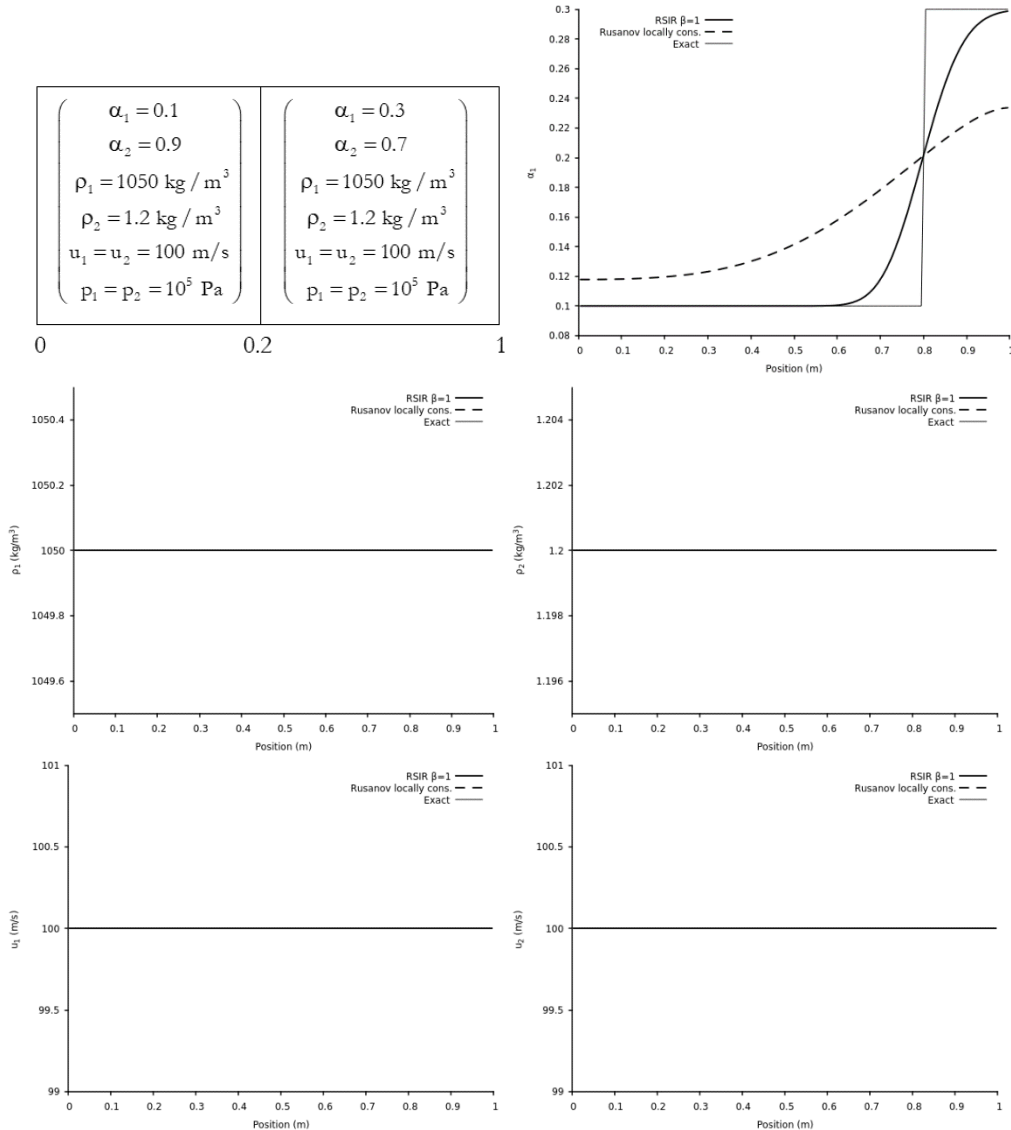


Figure III.7 – Results obtained by the new solver ($\beta=1$) for the computation of a contact discontinuity at rest. The computational domain involves 100 cells and the Godunov first-order scheme is used with $CFL=0.9$. Results are shown at time $t=6$ ms. The volume fraction discontinuity is well preserved and spurious pressure and velocity oscillations are absent.

Transport of the same volume fraction discontinuity is now considered in a flow in uniform pressure and velocity conditions. Corresponding results are shown in Figure III.8.



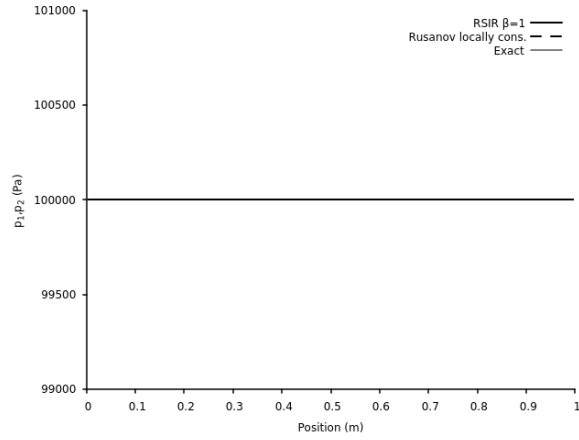
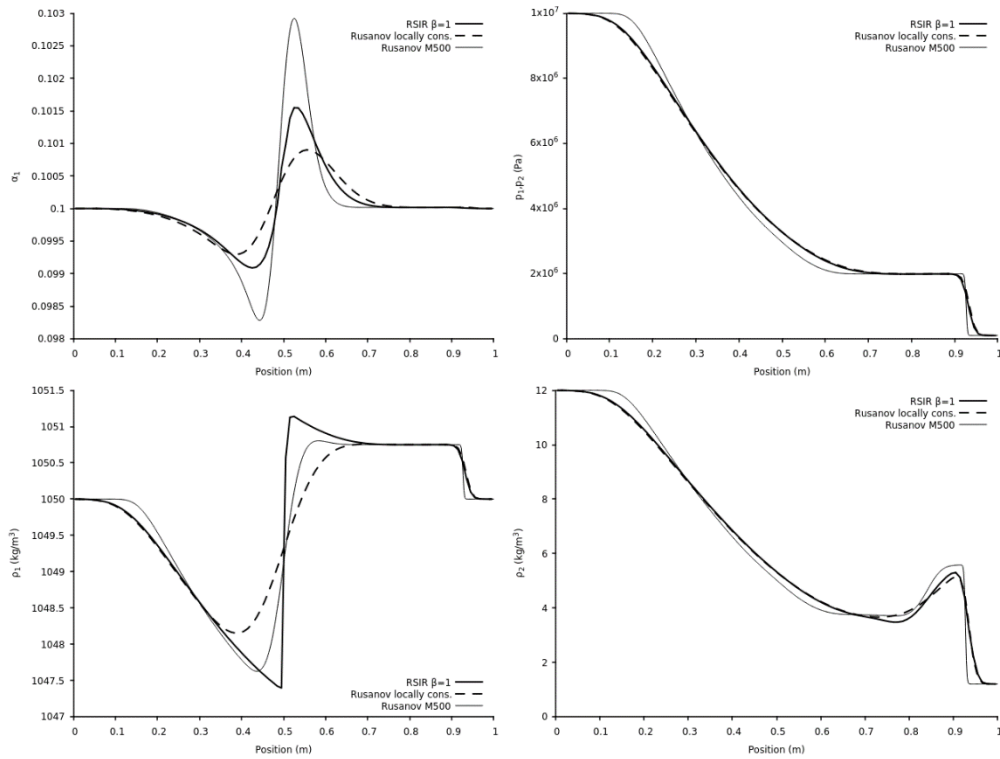


Figure III.8 – Results obtained by the new solver ($\beta=1$) for the computation of volume fraction discontinuity transport in a uniform pressure and velocity flow. The computational domain involves 100 cells and the Godunov first-order scheme is used with CFL=0.9. Results are shown at time $t=6$ ms.

The same two-phase shock tube test problem as in Figures III.2 and III.3, in the absence of drag force is now considered. The new method and the Rusanov solver are compared in Figure III.9.



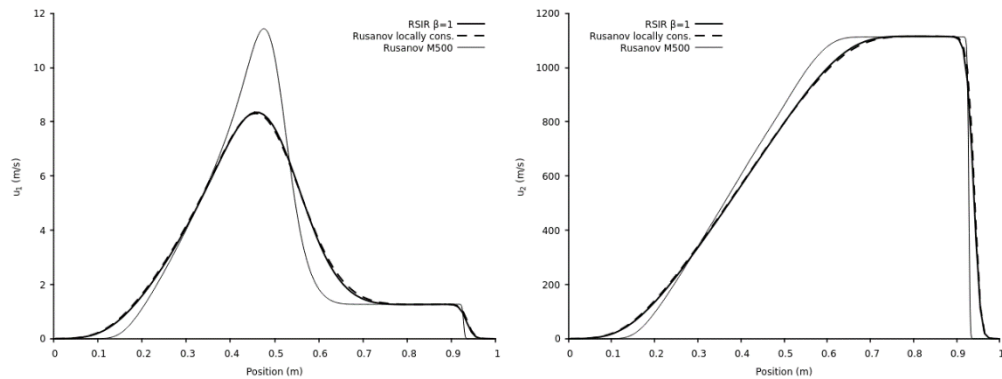


Figure III.9 – Comparison of the results obtained by the new solver ($\beta=1$) and the local conservative solver of Rusanov, both embedded in the Godunov first-order scheme with CFL=0.9. The various computations address the shock tube test presented in Figure III.2. 100 computational cells are used. Results are shown at time $t=300 \mu\text{s}$. Stiff pressure relaxation is used. With the RSIR method, significant improvements appear in the volume fraction and density profiles of the first phase. Indeed, the volume fraction solution with RSIR when 100 cells are used lies between the computed results of the Rusanov method with 100 and 500 cells.

The RSIR solver is consequently validated and improves accuracy of the Rusanov and HLL solvers. Also, it preserves volume fraction discontinuities at rest. Its capabilities are now illustrated on the computation of a challenging two-phase flow instability.

IV. Multi-D example: Particle jetting during radial explosion

When a spherical or cylindrical explosive charge is surrounded by a liquid layer or a granular particle bed, material dispersal occurs through particle jets having well-defined size. On the example shown in Figure IV.1, a cylindrical explosive charge is initially surrounded by a liquid layer.

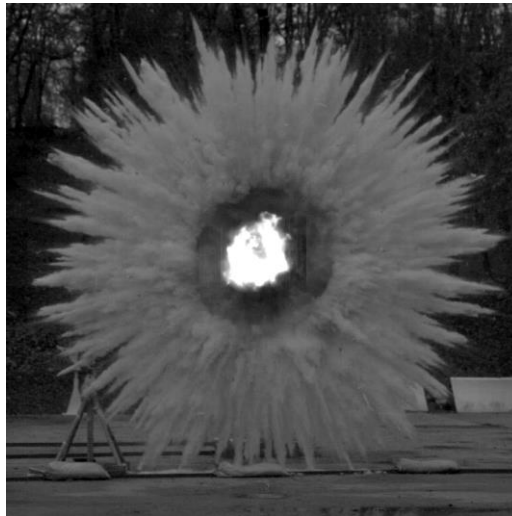


Figure IV.1 – A cylindrical explosive charge is initially surrounded by a liquid layer. When the charge explodes the liquid layer transforms to a cloud of droplets forming highly dynamical particle jets. Same jetting effects appear when the liquid is replaced by a granular layer. These jets are present in cylindrical and spherical dispersal explosions.

Gas expansion during explosion fragments the liquid layer to a cloud of droplets that form highly dynamical particle jets. The same observation is reported when a granular bed is used instead of a liquid layer. Dispersion is consequently clearly multidimensional in the sense that one-dimensional

computations result in significant errors in predicting presence of materials.

Experimental and numerical studies of this phenomenon have been carried out by Zhang et al. (2001), Milne et al. (2010), Frost (2010), Parrish and Worland (2010) to cite a few. Simplified situations have been considered in Rodriguez et al. (2013) and Xue et al. (2018). The explosive is replaced by a shock tube and the matter to disperse is placed between two plates, in a Hele-Shaw cell. Other simplified situations have been considered for example in McGrath et al. (2018), Osnes et al. (2018), Carmouze et al. (2018) to study possible clustering effects due to aerodynamic forces. It seems that jets' formation and size selection mechanism are still unidentified.

In the following a configuration like the one considered in Rodriguez et al. (2013) with a Hele-Shaw cell and a particle ring is studied. Typical results reported in Rodriguez's thesis are shown in Figure IV.2 at times 5 ms, 8 ms and 57 ms after rupture of the shock tube diaphragm, inducing shock wave and gas flow through a ring of flour particles.

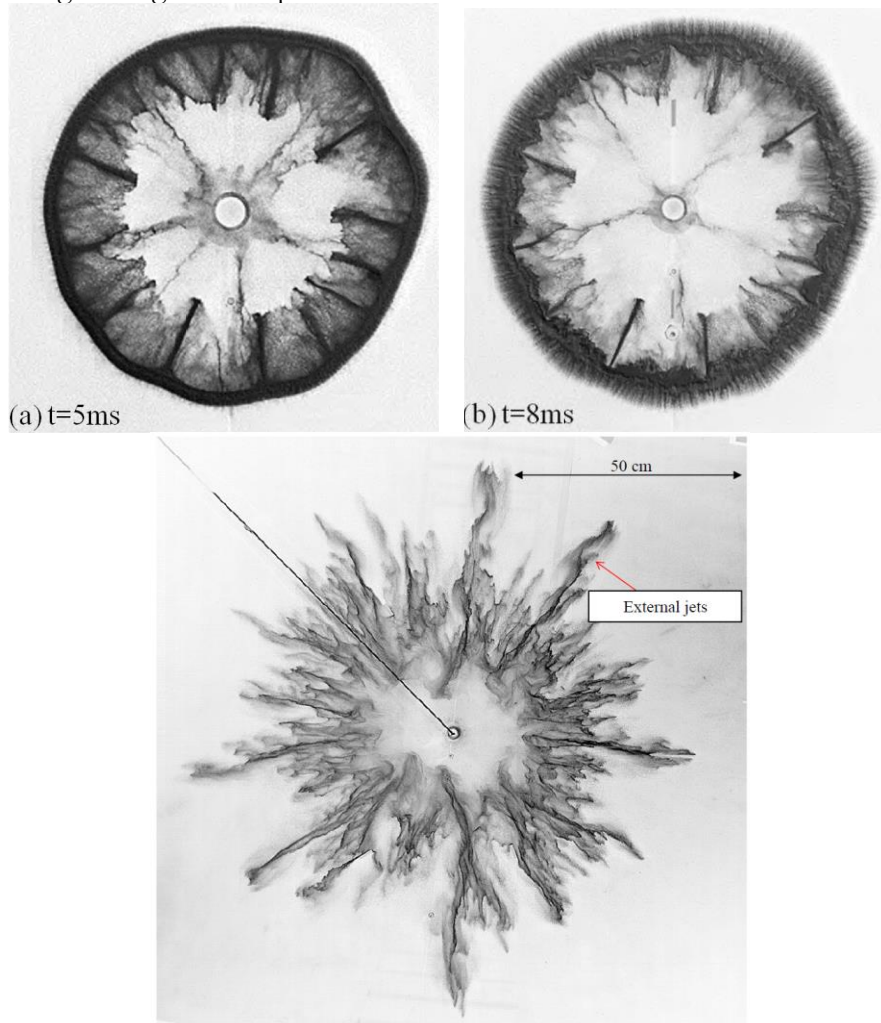


Figure IV.2 – Typical interfacial instabilities reported in Rodriguez's thesis and papers, as well as in Xue et al. (2018).

Impulsive motion of a particle ring by a gas flow induces well defined particle fingers flowing to the center direction, oppositely to the gas flow. At later times, here at 8 ms, short wavelength instabilities also appear at the external surface. As time evolves, external surface instabilities grow and become dominant, as shown in the third picture at time 57 ms.

Internal jets are thus observed at early times, followed by external ones at late times.

As reported by Rodriguez et al. (2013) and Xue et al. (2018), instabilities appear first at the inner interface and second at the outer one. Shape of these fingers is singular, in the sense that they do not

qualitatively compare to the Richtmyer-Meshkov instabilities or Rayleigh-Taylor ones, nor any other known instability. Indeed, mushroom type shape is observed with these two instabilities, while fingers are observed in the present context.

With the help of the new model and present RSIR solver, an attempt is made to reproduce at least qualitatively these instabilities. Former attempts by the authors were based on Marble (1963) model and failed to reproduce any, inner or outer, instability. In the present attempt, computations are based on flow model III.1 extended to 2D and resolved numerically in the DALPHADT© code on unstructured triangular cells. The Godunov-type method including non-conservative terms is extended to second order with the MUSCL-type method presented in Chiapolino et al. (2017).

Compared to the Marble model, the present one has a fundamental difference. Non-conservative terms are present in the momentum and energy equations. These non-conservative terms are often called ‘nozzling terms’ in reference to the Euler equations with variable cross section. We prefer however to interpret them as ‘differential drag force’. As shown for example in Figure III.9, phase 1 is set to motion as a result of these terms, in the absence of conventional drag force. Indeed, drag parameter λ is set to zero in these computations. As shown later, it seems that non-conservative terms are responsible for the appearance of these instabilities and size selection.

The computational domain and initial data are reported in Figure IV.3.

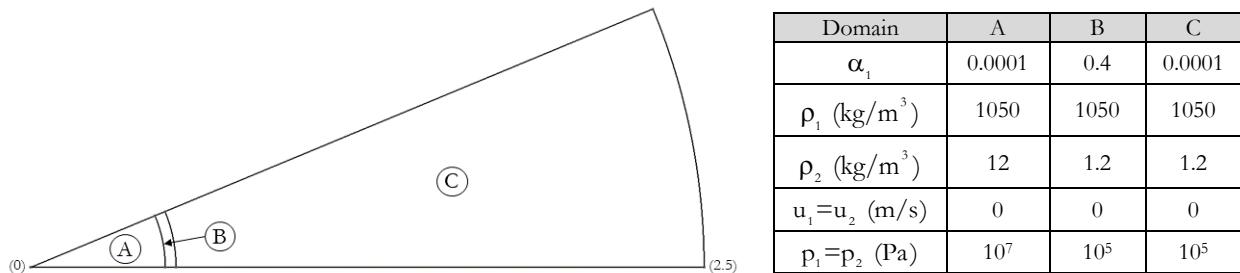


Figure IV.3 – Computational domain and initial data. The portion represents 1/16 of the complete disc with angle $\theta = \pi/8$. The domain denoted A corresponds to the high-pressure chamber, filled with gas. The domain denoted B represents the initial particle ring. It is located at radius 0.5 m and is 4-cm wide. The domain denoted C corresponds to the low-pressure chamber at atmospheric conditions initially.

Four different 2D meshes are used in the present contribution with 240,672 cells, 361,222 cells, 539,354 cells and 723,152 cells. The meshes are made of unstructured triangles and contains about 15, 20, 25 and 30 cells in the radial direction of the particles’ ring.

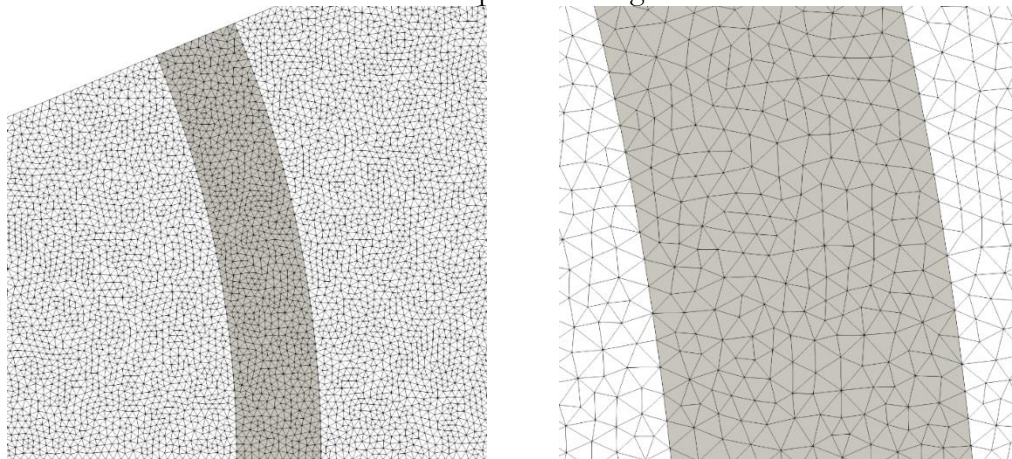


Figure IV.4 – Portion of the mesh used in the particle jetting computations focused on the particle bed. In the entire domain, 240,672 computational cells are used in the present figure for the sake of clarity. A close-up view of the mesh layout is depicted on the right. The use of triangular cells enables clear definition of the particle ring (dark zone). No mixed cell is present initially, meaning that no initial wavelength or perturbation is introduced.

As shown in Figure IV.4 the use of triangular cells enables clear definition of the particle ring boundaries, without mixed cell and associated grid roughness. No initial perturbation is present in the following computations. More precisely the particle volume fraction is initially uniform in the cloud. No arbitrary wavelength is introduced in the initial data.

Typical computed results are shown in Figures IV.5 and IV.6 and IV.7 at different times. Volume fraction contours are shown. These results show that the flow model reproduces, at least qualitatively both fingering instabilities issued from the inner and outer surfaces. In the present computations drag force is considered with a constant particle diameter (1 mm) and air kinematic viscosity ($18 \cdot 10^{-6}$ Pa.s). Drag force is modelled through Clift and Gauvin (1971) correlation,

$$\vec{F}_D = \frac{3}{8R_1} \alpha_1 C_d \rho_2 \|\vec{u}_2 - \vec{u}_1\| (\vec{u}_2 - \vec{u}_1),$$

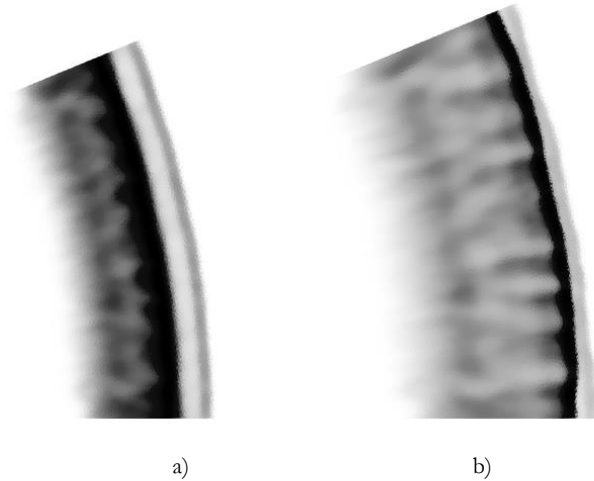
with,

$$C_d = \begin{cases} \frac{24}{Re_1} (1 + 0.15 Re_1^{0.687}) & \text{if } Re_1 < 800 \\ 0.438 & \text{otherwise} \end{cases}$$

$$\text{and } Re_1 = \frac{2R_1 \rho_2 \|\vec{u}_2 - \vec{u}_1\|}{\mu_2}.$$

Drag force \vec{F}_D is inserted in the right-hand side of the momentum equation of phase 1 and its opposite in phase 2. The power of this force $\vec{F}_D \cdot \vec{u}_1$ is inserted similarly in associated energy equations.

In the absence of drag effects, internal particle jets' selection is observed as well but quantitative differences appear at later times. Computed results at early times are shown in Figure IV.5.



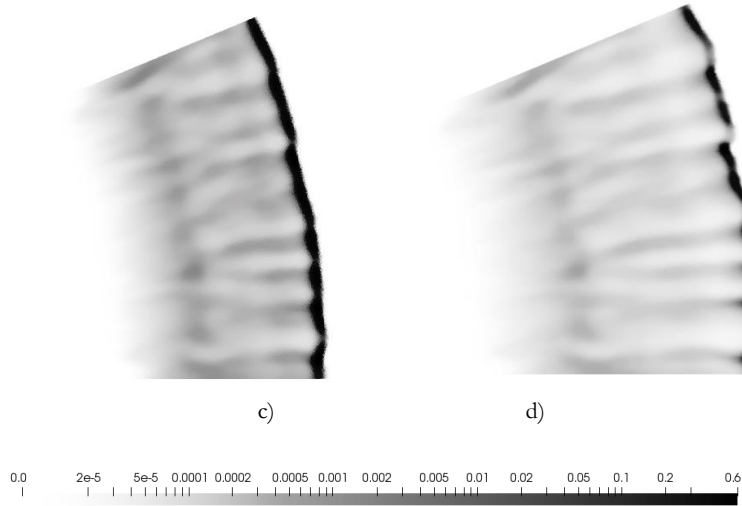


Figure IV.5 – Volume fraction contours of the dispersed phase for the particle jetting simulation, focused on the particle cloud at early times: (a) $t=0.6$ ms, (b) $t=0.84$ ms, (c) $t=1$ ms and (d) $t=1.3$ ms. In the present figure, the scale is adapted for each result for the sake of clarity. 723,152 cells are used with $CFL=0.5$. Results are obtained with the RSIR ($\beta=1$) solver embedded in the MUSCL scheme with Sweby’s limiter (1984) and $\Phi = 1.5$ in Eq. 3.17 of this reference. A compaction zone appears first in the cloud in the darkest zone. Particle jets develop at the inner interface and direct to the domain center. Their growth is visible by comparing their length in graphs (a) and (b). They qualitatively look like the instabilities observed in Figure IV.2 (a) and (b). Another front appears at the outer surface but appears more like a diffusion zone rather than the short wavelength instabilities visible in Figure IV.2 (b). Eventually the two fronts merge in graph (c) and the resulting front starts to destabilize in graph (d).

In Figure IV.5 internal jets appear and develop to the center domain direction. A compaction zone appears in the cloud and a detached front with low particle concentration also appears ahead of the compaction front. Noticeably, the compaction front in the darkest zone catches up the detached front and starts to destabilize. Evolution at intermediate times is reported in Figure IV.6.

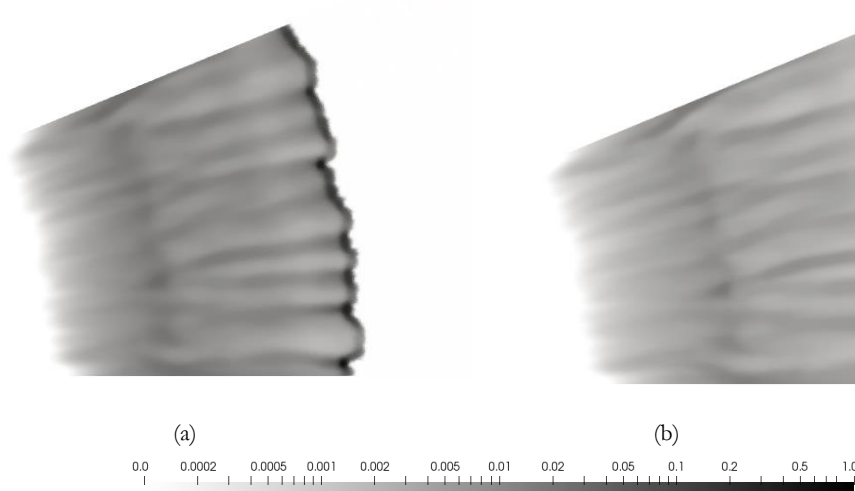


Figure IV.6 – Volume fraction contours of the dispersed phase for the particle jetting simulation, focused on the cloud at intermediate times: (a) $t=1.5$ ms and (b) $t=2.25$ ms. In the present figure, the scale is adapted for each result for the sake of clarity. Same computational parameters as those of Figure IV.5 are used as the results are extracted from the same computation. The compaction front and the detached one are now merged and destabilize. Particle concentration zones having cluster type shapes appear in graph (b). Inner jets are still present and keep on developing.

In Figure IV.6 the external front destabilizes, and relatively dense particle clusters appear. The inner front jets flowing to the domain center continue their development. Evolution at later times is reported in Figure IV.7.

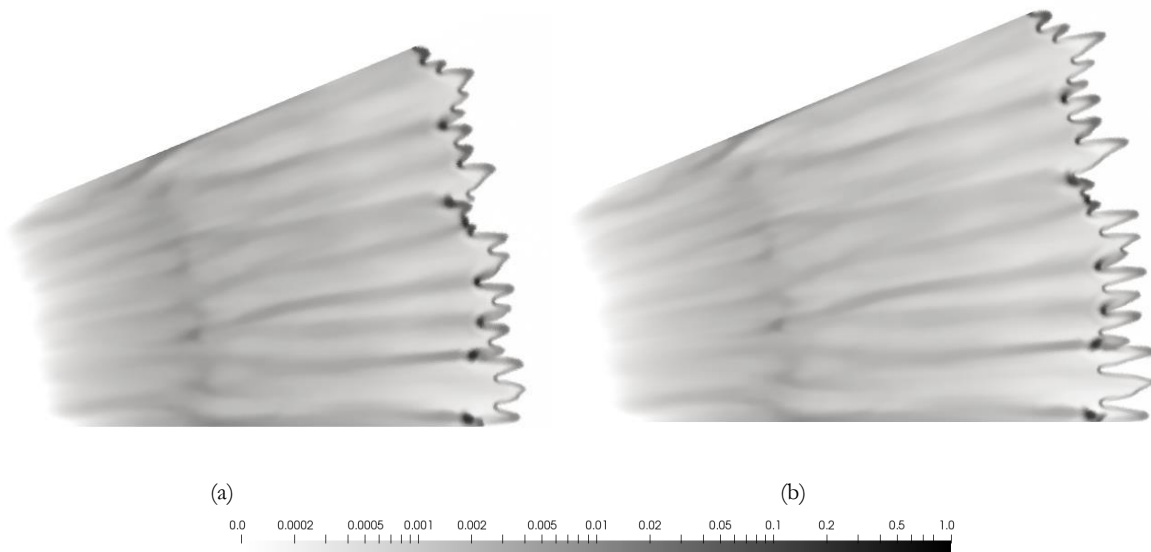


Figure IV.7 – Volume fraction contours of the dispersed phase for the particle jetting simulation, focused on the particle cloud at later times: (a) $t=3$ ms and (b) $t=3.75$ ms. In the present figure, the scale is adapted for each result for the sake of clarity. Same computational parameters as those of Figure IV.5 and IV.6 are used. External front instabilities are now created and develop. Dilution of the internal jets happens while external jets develop as a consequence of particle ‘dense’ zones created at intermediate times. External jets’ amplitude grows as seen by comparing results of graphs (a) and (b).

In Figure IV.7 external front instabilities are created and develop while internal ones tend to vanish. Although not precisely identified from the present numerical experiments, the formation mechanism of this fingering instability appears closely related to non-conservative terms. They play the role of a differential drag force, acting intensively at cloud boundaries and vanishing in the wake, when volume fraction gradients disappear.

At the modeling level, non-conservative terms present quite similar formulations to capillary ones (Brackbill et al., 1992, Perigaud and Saurel, 2005) except that curvature effects are absent in the present two-phase formulation. Another major difference is that cloud boundaries are obviously highly permeable in the present context, while interfaces are not permeable in conventional hydrodynamic instabilities, except those considering flames and phase transition, where low permeability is present compared to the present configuration.

In Figure IV.8, same numerical results are shown at different times in the entire computational domain with the same color map and scale, showing the evolution of the finger-like instabilities.



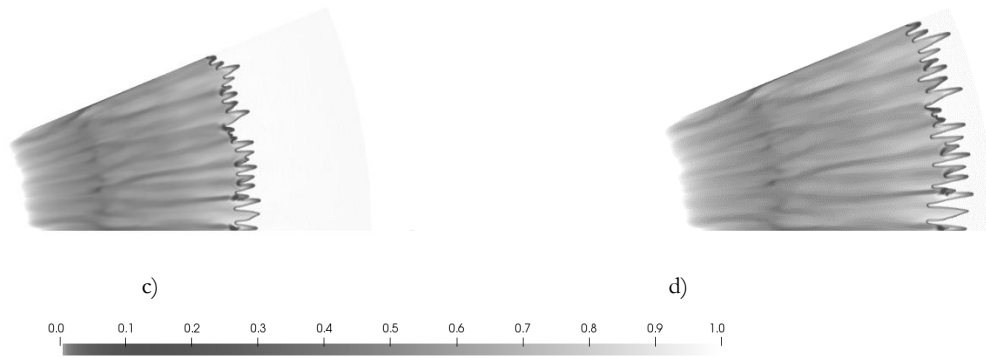


Figure IV.8 – Volume fraction contours of the dispersed phase for the particle jetting simulation. 723,152 cells are used with CFL=0.5. Results are obtained with the RSIR ($\beta=1$) solver embedded in the MUSCL scheme with Sweby’s limiter (1984) and $\Phi = 1.5$ in Eq. 3.17 of this reference. Results are shown at times $t=1.5$ ms (a), $t=3$ ms (b), $t=3.9$ ms (c) and $t=4.8$ ms (d).

In the following, we address spatial resolution effects. It appears that the number of created fingers does not depend on the mesh resolution. Indeed, as shown in Figure IV.9, the same number of fingers is created with four different meshes.

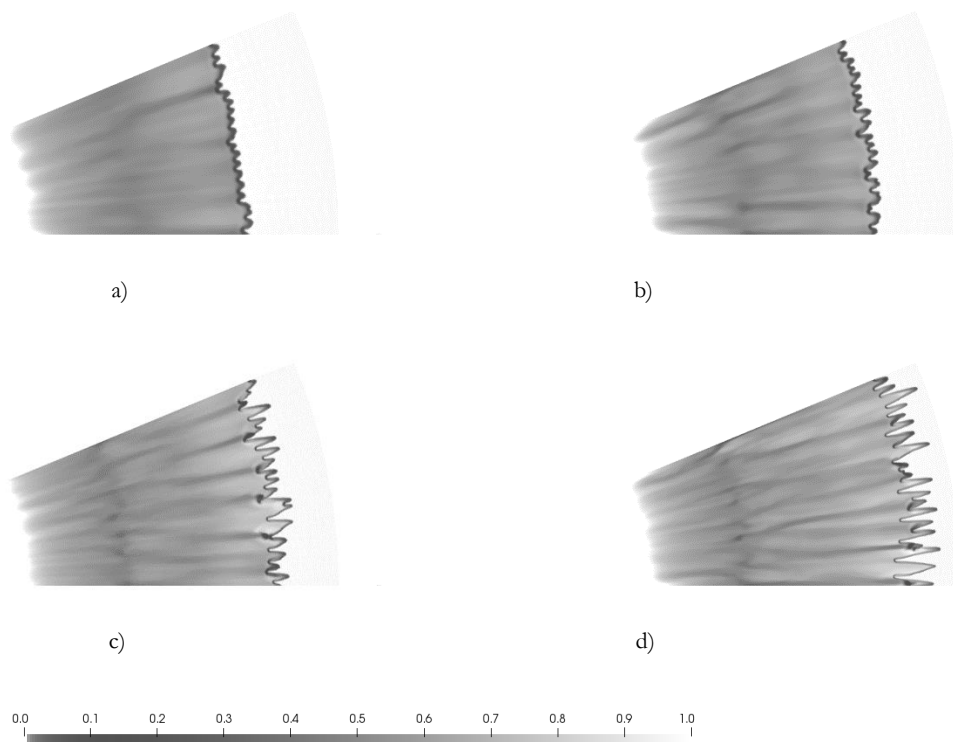


Figure IV.9 – Volume fraction contours of the dispersed phase for the particle jetting simulation. Study of mesh resolution effects. Results are obtained with the RSIR ($\beta=1$) solver embedded in the MUSCL scheme with Sweby’s limiter (1984) and $\Phi = 1.5$ in Eq. 3.17 of this reference and CFL=0.5. Results are shown at times $t=4.8$ ms with four different meshes, 240,000 cells (a), 360,000 cells (b), 540,000 cells (c) and 720,000 cells (d).

Obviously, mesh resolution influences jets' shape and length, as numerical diffusion is present. However, it does not change the number of jets and their qualitative shape, meaning that this instability is 'robust' and that the flow model and present numerical method seem appropriate for their study.

V. Conclusion

A Riemann solver with internal reconstruction (RSIR) has been built as an extension of the Linde (2002) solver. It has been first developed for the Euler equations. Its accuracy and robustness appear similar to the HLLC solver, while being not as systematic. The method has been secondly extended to a two-phase non-equilibrium model developed by the authors. This model presents serious difficulties as it is weakly hyperbolic and valid only in the limit of stiff pressure relaxation, rendering solutions non self-similar. Thanks to the RSIR approach, a low dissipation solver has been developed. It has been validated against solutions obtained with a more conventional, but dissipative solver. The new method has been applied in the last section to a difficult problem of fingering instability in granular media and has shown possible explanation of the instability formation mechanism. Extra work is still needed in this special two-phase flow topic to achieve understanding of this instability. Regarding the Riemann solver, it seems flexible for many applications where most of the physics is governed by the two extreme waves and an intermediate one.

Acknowledgements. Part of this work has been carried out in the framework of the ANR project SUBSUPERJET ANR-14-CE22-0014. The authors are particularly grateful to the anonymous referees for the quality of their remarks and analysis that helped to improve the quality of the present work.

References

- Allaire, G., Clerc, S., & Kokh, S. (2002) A five-equation model for the simulation of interfaces between compressible fluids. *Journal of Computational Physics*, 181(2), 577-616
- Balsara, D. S. (2012) A two-dimensional HLLC Riemann solver for conservation laws: Application to Euler and magnetohydrodynamic flows. *Journal of Computational Physics*, 231(22), 7476-7503
- Baer, M. R., & Nunziato, J. W. (1986) A two-phase mixture theory for the deflagration-to-detonation transition (DDT) in reactive granular materials. *International Journal of Multiphase Flow*, 12(6), 861-889
- Brackbill, J. U., Kothe, D. B., & Zemach, C. (1992) A continuum method for modeling surface tension. *Journal of Computational Physics*, 100(2), 335-354
- Bouchut, F., Jin, S., & Li, X. (2003) Numerical approximations of pressureless and isothermal gas dynamics. *SIAM Journal on Numerical Analysis* 41(1), 135-158
- Carmouze, Q., Fraysse, F., Saurel, R., & Nkonga, B. (2018) Coupling rigid bodies motion with single phase and two-phase compressible flows on unstructured meshes. *Journal of Computational Physics*, 375, 1314-1338
- Chiapolino, A., Saurel, R., & Nkonga, B. (2017) Sharpening diffuse interfaces with compressible fluids on unstructured meshes. *Journal of Computational Physics*, 340, 389-417
- Clift, R., & Gauvin, W. H. (1971) Motion of entrained particles in gas streams. *The Canadian Journal of Chemical Engineering*, 49(4), 439-448
- Cocchi, J. P., Saurel, R., & Loraud, J. C. (1998). Some remarks about the resolution of high velocity flows near low densities. *Shock Waves*, 8(2), 119-125
- Davis, S., (1988) Simplified second-order Godunov-type methods. *SIAM Journal on Scientific and Statistical Computing*, 9(3), 445-473
- Forestier, A., & Le Floch, P. (1992) Multivalued solutions to some non-linear and non-strictly hyperbolic systems. *Japan journal of industrial and applied mathematics*, 9(1), 1
- Frost (2010) Jet formation during explosive particle dispersal. *Proceedings of the 21st Int. Symp. on Military Aspects of Blast and Shocks*, Jerusalem, October 3-4
- Furfaro, D., & Saurel, R. (2015) A simple HLLC-type Riemann solver for compressible non-equilibrium two-phase flows. *Computers & Fluids*, 111, 159-178

- Gavrilyuk, S. L., Favrie, N., & Saurel, R. (2008) Modelling wave dynamics of compressible elastic materials. *Journal of computational physics*, 227(5), 2941-2969
- Kapila, A. K., Menikoff, R., Bdzil, J. B., Son, S. F., & Stewart, D. S. (2001) Two-phase modeling of deflagration-to-detonation transition in granular materials: Reduced equations. *Physics of Fluids*, 13(10), 3002-3024
- Lallemand, M. H., & Saurel, R. (2000) Pressure relaxation procedures for multiphase compressible flows. INRIA Report
- Lhuillier, D., Chang, C. H., & Theofanous, T. G. (2013) On the quest for a hyperbolic effective-field model of disperse flows. *Journal of Fluid Mechanics*, 731, 184-194
- Linde, T. (2002) A practical, general-purpose, two-state HLL Riemann solver for hyperbolic conservation laws. *International Journal for Numerical Methods in Fluids*, 40(3-4), 391-402.
- Marble, F.E (1963) Dynamics of a gas containing small solid particles. *Combustion and Propulsion (5th AGARD Colloquium)*, 175, Pergamon Press
- Milne, A., Parrish, C. and Worland, I. (2010) Dynamic fragmentation of blast mitigants. *Shock Waves* 20: 41-51
- McGrath, T., Clair, J. S., & Balachandar, S. (2018) Modeling compressible multiphase flows with dispersed particles in both dense and dilute regimes. *Shock Waves*, 28(3), 533-544
- Miyoshi, T., & Kusano, K. (2005) A multi-state HLL approximate Riemann solver for ideal magnetohydrodynamics. *Journal of Computational Physics*, 208(1), 315-344
- Osnes, A. N., Vartdal, M., & Reif, B. P. (2018) Numerical simulation of particle jet formation induced by shock wave acceleration in a Hele-Shaw cell. *Shock Waves*, 28(3), 451-461
- Parrish and Worland (2010) Dynamic jet formation from mitigation materials. *Proceedings of the 21st Int. Symp. on Military Aspects of Blast and Shocks*, Jerusalem, October 3-4
- Perigaud, G., & Saurel, R. (2005) A compressible flow model with capillary effects. *Journal of Computational Physics*, 209(1), 139-178
- Petitpas, F., Saurel, R., Franquet, E., & Chinnayya, A. (2009) Modelling detonation waves in condensed energetic materials: Multiphase CJ conditions and multidimensional computations. *Shock waves*, 19(5), 377-401
- Rodriguez, V., Saurel, R., Jourdan, G., & Houas, L. (2013) Solid-particle jet formation under shock-wave acceleration. *Physical Review E*, 88(6), 063011
- Rusanov, V. V. E. (1961) The calculation of the interaction of non-stationary shock waves and obstacles. *USSR Computational Mathematics and Mathematical Physics* 1(2), 304-320
- Saurel, R., Daniel, E., & Loraud, J. C. (1994) Two-phase flows - Second-order schemes and boundary conditions. *AIAA Journal*, 32(6), 1214-1221
- Saurel, R., & Abgrall, R. (1999) A multiphase Godunov method for compressible multifluid and multiphase flows. *Journal of Computational Physics*, 150(2), 425-467
- Saurel, R., Chinnayya, A. & Carmouze, Q., (2017a) Modeling compressible dense and dilute two-phase flows. *Physics of Fluids*, 29(6), 063301
- Saurel, R., Fraysse, F., Furfaro, D., & Lapebie, E. (2017b) Multiscale multiphase modeling of detonations in condensed energetic materials. *Computers & Fluids*, 159, 95-111
- Saurel, R., & Pantano-Rubio, C. (2018) Diffuse interface capturing methods for compressible two-phase flow. *Annual Review of Fluid Mechanics*, 50(1), 105-130
- Sweby, P. (1984) High resolution schemes using flux limiters for hyperbolic conservation laws. *SIAM Journal on Numerical Analysis*, 21(5), 995-1011
- Toro, E. F., Spruce, M., & Speares, W. (1994) Restoration of the contact surface in the HLL-Riemann solver. *Shock waves*, 4(1), 25-34
- Toro, E.F. (2009) *Riemann solvers and numerical methods for fluid dynamics. A practical introduction*. Third edition. Springer-Verlag, Berlin Heidelberg, 2009. Book (724 pages). ISBN 978-3-540-25202-3
- Toro, E.F (2019) The HLLC Riemann Solver: A Review. *Shock Waves*, doi.org/10.1007/s00193-019-00912-4
- Xue, K., Du, K., Shi, X., Gan, Y. and Bai, C. (2018) Dual hierarchical particle jetting of a particle ring undergoing radial explosion. *Soft Matter*, 2018,14, 4422
- Wood, A. B. (1930) *A Textbook of Sound*. G. Bell and Sons Ltd., London
- Woodward, P., & Colella, P. (1984) *The Numerical Simulation of Two-Dimensional Fluid with Strong Shocks*.

- Journal of Computational Physics, 54, 115-173
- Zeldovich, Y.B. (1970) Gravitational instability: An approximate theory for large density perturbations. *Astron. Astrophys*, 5, 84–89
- Zhang, F., Frost, D.L., Thibault, P.A. and Murray, S.B. (2001) Explosive dispersal of solid particles. *Shock Waves* 10: 431-443